

Gas Separation

Zitierweise: *Angew. Chem. Int. Ed.* **2021**, *60*, 10304–10310

Internationale Ausgabe: doi.org/10.1002/anie.202100342

Deutsche Ausgabe: doi.org/10.1002/ange.202100342

A Rod-Packing Hydrogen-Bonded Organic Framework with Suitable Pore Confinement for Benchmark Ethane/Ethylene Separation

Xu Zhang⁺, Jia-Xin Wang⁺, Libo Li, Jiyan Pei, Rajamani Krishna, Hui Wu, Wei Zhou, Guodong Qian, Banglin Chen* and Bin Li*

Abstract: For the separation of ethane from ethylene, it remains challenging to target both high C₂H₆ adsorption and selectivity in a C₂H₆-selective material. Herein, we report a reversible solid-state transformation in a labile hydrogen-bonded organic framework to generate a new rod-packing desolvated framework (ZJU-HOF-1) with suitable cavity spaces and functional surfaces to optimally interact with C₂H₆. ZJU-HOF-1 thus exhibits simultaneously high C₂H₆ uptake (88 cm³ g⁻¹ at 0.5 bar and 298 K) and C₂H₆/C₂H₄ selectivity (2.25), which are significantly higher than those of most top-performing materials. Theoretical calculations revealed that the cage-like cavities and functional sites synergistically „match“ better with C₂H₆ to provide stronger multipoint interactions with C₂H₆ than C₂H₄. In combination with its high stability and ultralow water uptake, this material can efficiently capture C₂H₆ from 50/50 C₂H₆/C₂H₄ mixtures in ambient conditions under 60% RH, providing a record polymer-grade C₂H₄ productivity of 0.98 mmol g⁻¹.

Introduction

Ethylene (C₂H₄) is a key feedstock for many chemicals and polymers in the chemical industry and is primarily derived from naphtha or ethane cracking.^[1,2] However, steam

crackers do not produce pure C₂H₄ (≥ 99.95%, polymer grade), in which ethane (C₂H₆) is inevitably existed as a major byproduct. The separation of C₂H₆ from C₂H₄ is thereby a critical process to yield polymer-grade C₂H₄ for polymer production. At present, it is mainly accomplished by means of cryogenic distillation under harsh conditions (typically at 5–28 bar and 180–258 K), which represents one of the most energy-intensive processes. The energy consumption for such separation is estimated to be about 7.3 GJ per tonne of ethylene.^[3,4] To replace traditional cryogenic distillation, adsorptive separation technologies based on porous materials attract particular interest because of their great potential to provide tremendous energy savings.^[5] Such separation can be implemented by either ethane- or ethylene-selective adsorbents; however, ethane-selective materials are more desired because of the simplicity of being able to produce ethylene directly at the outlet.^[6,7]

Since ethane has a higher polarizability than ethylene, dispersion and induction interactions would make major contributions in C₂H₆-selective adsorbents,^[8] so an adsorbent material with a pore structure enriched with nonpolar/inert surfaces (e.g., featuring aromatic or aliphatic moieties) may favor the preferential adsorption of C₂H₆ over C₂H₄. In this regard, the emerging hydrogen-bonded organic frameworks (HOFs) are of particular interest to be developed as C₂H₆-selective adsorbents.^[9,10] HOFs are formed from purely organic building blocks through intermolecular hydrogen bonds (H-bonds).^[11–14] This metal-free nature endows HOFs with native nonpolar/inert pore surfaces to directly produce the desired C₂H₆-selective materials. Owing to the soft and flexible H-bonds, HOFs hold some inherent advantages such as high solution processability, easy purification, and facile regeneration and healing by simple recrystallization. Moreover, HOF materials can be highly crystalline that benefits not only structural determination but also the investigation of structure–property relationship. These attractive merits make the exploitation of porous HOFs as C₂H₆-selective adsorbents become very attractive. However, the major drawback of HOFs is their structural fragility because of the weak nature of H-bonds, making their frameworks oftentimes collapse upon removal of solvent molecules.^[15] It is also very difficult to precise control over pore size and functional sites in HOFs to strongly interact with gas molecules,^[9,10] which has always limited their separation performance. It is therefore not surprising that the research on robust HOFs for gas separation is still at the comparatively early stage.^[16,17] To date, only few porous HOFs have been established for the important hydrocarbon separations with quite limited separation per-

[*] Dr. X. Zhang,^[†] J.-X. Wang,^[†] J. Pei, Prof. G. Qian, Prof. B. Li
 State Key Laboratory of Silicon Materials
 School of Materials Science and Engineering, Zhejiang University
 Hangzhou 310027 (China)
 E-Mail: bin.li@zju.edu.cn



Prof. L. Li
 College of Chemistry and Chemical Engineering
 Taiyuan University of Technology
 Taiyuan 030024, Shanxi (China)

Prof. B. Chen
 Department of Chemistry, University of Texas at San Antonio
 One UTSA Circle, San Antonio, TX 78249-0698 (USA)
 E-Mail: banglin.chen@utsa.edu

Prof. R. Krishna
 Van't Hoff Institute for Molecular Sciences, University of Amsterdam
 Science Park 904, 1098 XH Amsterdam (The Netherlands)

Dr. H. Wu, Dr. W. Zhou
 NIST Center for Neutron Research
 National Institute of Standards and Technology
 Gaithersburg, MD 20899-6102 (USA)

[†] These authors contributed equally to this work.

 Supporting information and the ORCID identification number(s) for the author(s) of this article can be found under:
 <https://doi.org/10.1002/anie.202100342>.

formance.^[18–20] Despite a great challenge, we recently succeeded in realizing a robust HOF material (HOF-76a) for selective separation of C_2H_6/C_2H_4 .^[18] While this material exhibits a moderate C_2H_6/C_2H_4 selectivity, the large one-dimensional pores and the lack of strong C_2H_6 adsorption sites lead to a weak binding affinity and thus poor C_2H_6 uptake, largely delimiting the productivity of the desired C_2H_4 product.

A chemical separation benefits from both uptake capacity and adsorption selectivity and can be most efficient when a material excels in both aspects; however, it is very difficult to target a material with both high values (so-called trade-off).^[21] To realize both high gas selectivity and adsorption uptake for C_2H_6/C_2H_4 separation, an ideal adsorbent should have suitable pore/cavity sizes and functional surfaces to simultaneously enforce the preferential adsorption of C_2H_6 over C_2H_4 but without sacrificing moderate pore volumes or surface areas to take up large amount of C_2H_6 molecules. However, from the structural point of view, there commonly exists a trade-off between pore dimensions and pore volumes in porous materials.^[22,23] For example, pore dimensions that match with small gas molecules often correlate to small pore volumes, which in turn result in low uptakes. Conversely, high pore volumes typically stem from large pores, which cannot discriminate the molecules with similar sizes. It is still

a daunting challenge for the community to design and realize ideal adsorbents to meet the above mentioned criteria, especially for the immature HOFs. Herein, we report a unique rod-packing HOF material (ZJU-HOF-1, Figure 1) featuring the suitable cavity sizes (4.6 Å) and functional surfaces, which can meet those mentioned criteria for benchmark C_2H_6/C_2H_4 separation. The activated ZJU-HOF-1 shows a relatively high BET surface area of $1465\text{ m}^2\text{ g}^{-1}$ to secure enough pore spaces for high C_2H_6 uptake. Owing to the rod-packing configuration and threefold interpenetration, ZJU-HOF-1 features numerous small cage-like cavities decorated by multipoint functional sites that match better with the size/shape of C_2H_6 molecule and thus facilitate closer contacts with C_2H_6 . This unique pore confinement thus results in a rare combination of simultaneously high C_2H_6 uptake ($88\text{ cm}^3\text{ g}^{-1}$ at 0.5 bar and 298 K) and C_2H_6/C_2H_4 selectivity (2.25) observed in ZJU-HOF-1. Importantly, this material is also chemically stable and shows an ultralow water uptake at 60% RH to avoid co-adsorption of water. Breakthrough experiments confirmed that ZJU-HOF-1 exhibits the record-high C_2H_4 productivity of 0.98 mmol g^{-1} (or 21.9 L kg^{-1}) for both dry and humid (60% RH) C_2H_6/C_2H_4 mixtures at 298 K and 1.01 bar, a value higher than that of $Fe_2(O_2)(\text{dobdc})$ (0.86 mmol g^{-1}), the benchmark material for C_2H_6/C_2H_4 separation in MOFs.

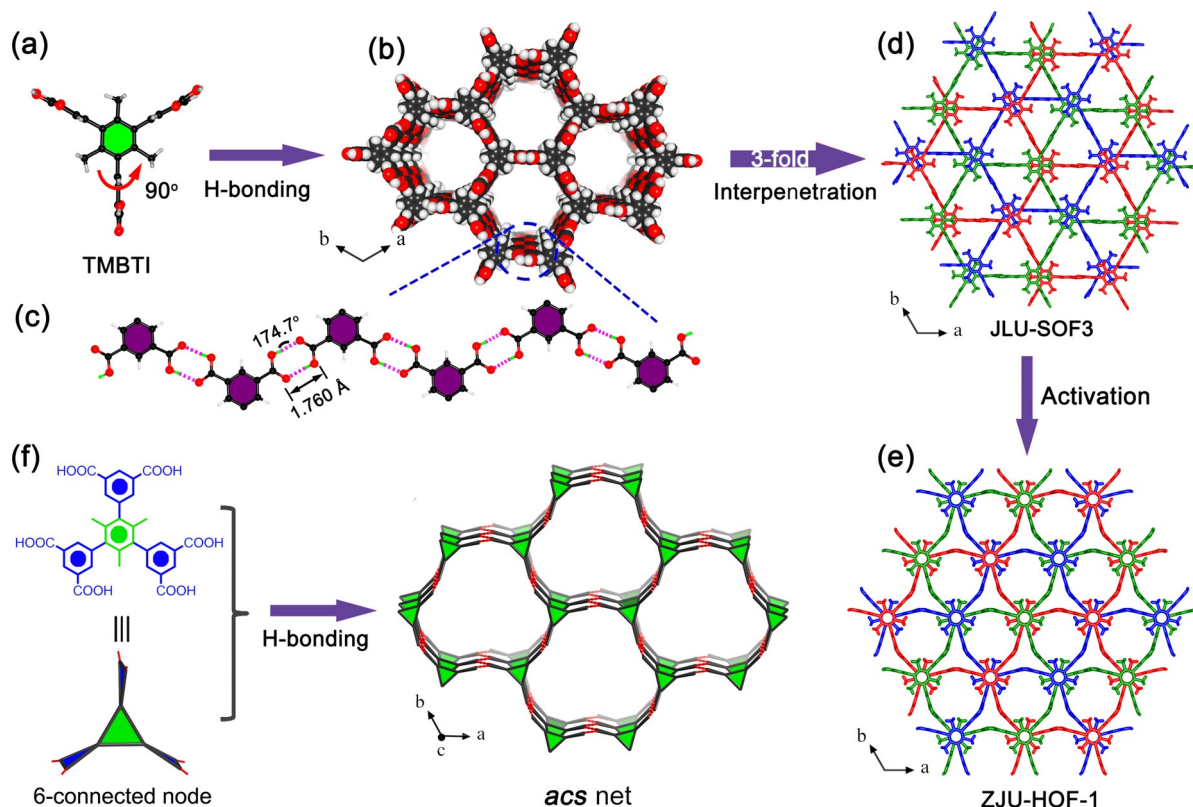


Figure 1. a) The structure of TMBTI. b) The single network constructed by TMBTI molecules. c) A rod-shaped H-bonded chain formed by meta-benzenedicarboxylic motifs along the c axis. d) The threefold-interpenetrated structure of JLU-SOF3. e) The modeled structure of ZJU-HOF-1 upon activation, revealing an obvious structural transformation between JLU-SOF3 and ZJU-HOF-1. f) The acs topology of ZJU-HOF-1 (red dotted lines represent H-bonds). The CCDC number can be found in the Supporting Information.

Results and Discussion

The hexacarboxylate ligand 2,4,6-trimethylbenzene-1,3,5-triylisophthalate (TMBTI) was simply prepared through a multistep reaction procedure (Scheme S1, Supporting Information). Slow evaporation of an ethyl ether solution into a THF solution of TMBTI in two weeks afforded the colorless stick-like crystals. During our exploration of the activated ZJU-HOF-1, the structure of the as-synthesized HOF (JLU-SOF3) was independently reported for different properties.^[13c] Single crystal X-ray diffraction analysis revealed that JLU-SOF3 crystallizes in a hexagonal $P\bar{6}2c$ space group with a hydrogen-bonded 3D network (Figure 1). Due to the steric hindrance of methyl groups, the dihedral angle of each outer phenyl ring relative to the center phenyl ring in TMBTI molecule is about 90° (Figure 1a). This feature enables the adjacent *meta*-benzenedicarboxylate motifs from different TMBTI to form 1D infinite rod-shaped H-bonding chains along the *c* axis (Figure 1c), which are further linked by the center phenyl ring to construct the 3D rod-packing framework (Figure 1b). The O–H...O distance and angle are 2.610/2.599 Å and 174.7° , respectively. If the TMBTI is considered as a six-connected node, JLU-SOF3 possesses the *acs* $\{4^96^6\}$ topology (Figure S7). Closer inspection of the structure reveals that six discrete TMBTI molecules form a six-membered ring in a hexagon pore conformation with a large window size of 22.7 Å. This large pore nature of single network can lead to interpenetration, wherein three identical frameworks interpenetrate each other through the ring-like window along the *c* axis (Figure 1d).

When the as-synthesized sample was desolvated in high vacuum to generate the activated sample (ZJU-HOF-1), we found that there exist obvious changes in the PXRD patterns between JLU-SOF3 and ZJU-HOF-1 (Figure S8). This clearly indicates that a structural transformation occurs during this activation, however, which was ignored in the reported literature. Great efforts have been made to elaborately

investigate the new structure of the activated ZJU-HOF-1. Despite extensive attempts, we were not able to obtain high-quality single crystals of ZJU-HOF-1 for single-crystal X-ray diffraction studies (Figure S9) and thus structural determination was conducted by powder diffractometry. On the basis of the PXRD data, we first identified a new symmetry of hexagonal $P\bar{6}c2$ space group for ZJU-HOF-1 crystal. With the symmetry and the overall network connection known, we thus modeled its structure straightforwardly and further optimized the structure based on DFT calculations (see Supporting Information for more details).^[24] The structure model is shown in Figure 1e, which has different unit cell parameters with JLU-SOF3 (Table S4). The simulated PXRD pattern of this structural model agrees excellently with the experimental data (Figure S10), strongly supporting its validity. Detailed structure information of ZJU-HOF-1 is provided in Tables S3 and S4.

To further probe the structural transformation from JLU-SOF3 to ZJU-HOF-1, the nudged elastic band calculations were performed to find the minimum energy path of the structural transition. An animation consisting of structure snapshots along the minimal energy path shows clearly how the JLU-SOF3 framework evolves to the structure of ZJU-HOF-1 (see the movie in the Supporting Information). During this process, the different nets are obviously smoothing along the *ab* plane to make the center phenyl rings of TMBTI molecules from adjacent nets coincide with each other, accompanying a slight rotation (15°) along the *c* axis for every monomer molecular. This transformation induces a slight structure contraction (5.43% by volume), leading to a new symmetry and uniform pores in ZJU-HOF-1 (Figure 2a). The framework of ZJU-HOF-1 still holds a threefold interpenetration with the same *acs* topology (Figure 1f and Figure S10, Supporting Information). The O–H...O distance (2.564 Å) on the rod-shaped H-bonded chains along the *c* axis is slightly shorter than that in ZJU-HOF-1 (Figure 2c). As depicted in Figure 2b, ZJU-HOF-1 exhibits open triangular-

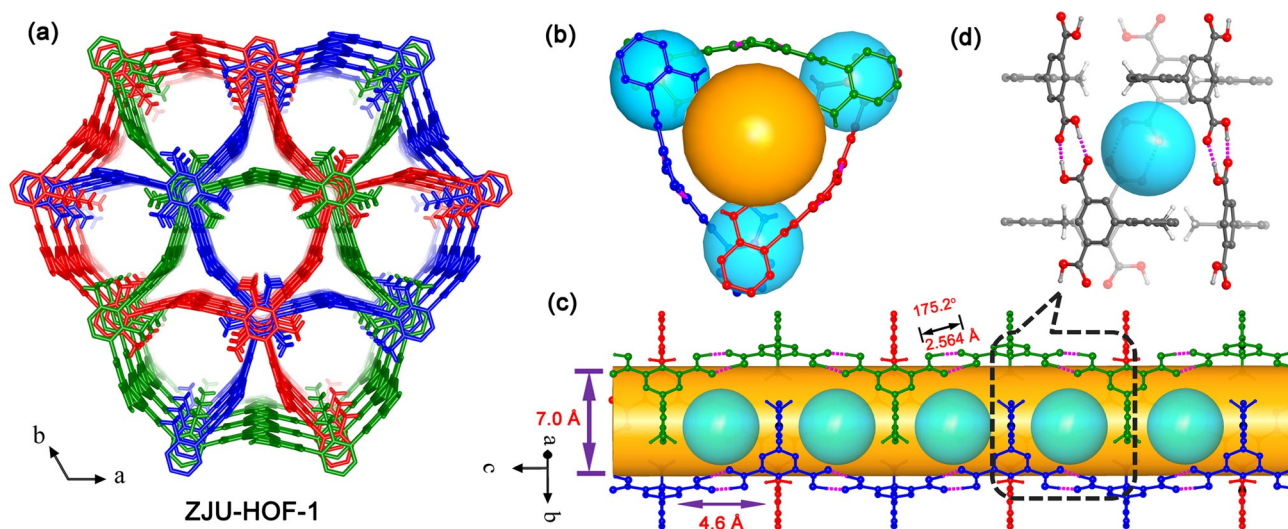


Figure 2. a) The threefold-interpenetrated structure of ZJU-HOF-1. b) The triangular pore channel (7.0 Å) and three intercrossed small pockets around the corners of the triangular-like channel. c) View of the small pockets stacked along the *c* axis, with a diameter of 4.6 Å. d) Depiction of one pocket constructed by two stacked phenyl rings and four carboxylate groups (C, dark gray; O, red; H, white).

like pore channels with a diameter of 7.0 Å along the *c* axis, which are large enough for both C₂H₄ and C₂H₆ molecules to enter the pores. Due to the rod-packing configuration and threefold interpenetration, there produces numerous small cage-like pockets around the corner of the triangular channels (Figure 2b,c). Each of such small pockets is constructed by two stacked phenyl rings and four carboxylate groups with a diameter size of 4.6 Å (Figure 2d), which matches better with the larger C₂H₆ molecule (4.4 Å) than C₂H₄ (4.1 Å). These optimized pocket sizes and pore surfaces of functional O atoms thus exhibit the potential to provide more suitable pore confinement effects toward C₂H₆ molecule.

The chemical stability and structural transformation between JLU-SOF3 and ZJU-HOF-1 were investigated at different conditions, monitored by PXRD patterns. As revealed in Figures S12 and S13, the framework of JLU-SOF3 can gradually transform to ZJU-HOF-1 under removal of solvent molecules upon air exposure, heating or vacuum degassing. Conversely, the framework of ZJU-HOF-1 can be reversibly converted to JLU-SOF3 when soaking the sample into the Et₂O or H₂O solution (Figure S14). To examine the chemical stability, the as-synthesized samples were treated in water, HCl (pH 1) and NaOH (pH 10) solutions at room temperature (RT). After two days, the framework can retain its structural integrity as evidenced by PXRD patterns and SEM images (Figures S15 and S16), revealing its highly chemical stabilities.

The permanent porosity of ZJU-HOF-1 was established by nitrogen (N₂) gas sorption experiments at 77 K. As shown in Figure 3a, ZJU-HOF-1 can adsorb a large amount of N₂

(386 cm³ g⁻¹) at 77 K and 1 bar. The BET surface area and pore volume of ZJU-HOF-1 were calculated to be moderate high of 1465 m² g⁻¹ and 0.60 cm³ g⁻¹, respectively. The pore size distribution, determined by the Horvath–Kawazoe model, shows two types of pores in the range of 5–9 Å, consistent well with the results obtained from the crystal structure. After immersing in water, HCl and NaOH solutions for 2 days, the reactivated ZJU-HOF-1 samples show no obvious decrease on N₂ uptakes at 77 K (Figure S19).

Single-component adsorption isotherms of C₂H₆ and C₂H₄ for ZJU-HOF-1 were examined at both 273 K and 298 K up to 1 bar. As shown in Figures 3b and S20, ZJU-HOF-1 shows an obviously preferential adsorption of C₂H₆ over C₂H₄ at both temperatures. The uptake amount of C₂H₆ (109 cm³ g⁻¹) at 298 K and 1 bar is notably higher than that of C₂H₄. When compared with HOF-76a, ZJU-HOF-1 exhibits a much steeper and higher C₂H₆ uptake in the whole range of 1 bar (Figure 3c). At a partial pressure of 0.5 bar for 50/50 C₂H₆/C₂H₄ separation, ZJU-HOF-1 displays an extremely high C₂H₆ uptake of 88 cm³ g⁻¹, 2.3 times higher than that of HOF-76a (38 cm³ g⁻¹),^[18] indicating its significantly enhanced C₂H₆ capture capacity (Figure 3c). This can be well explicated by the experimental isosteric heat of adsorption (*Q*_{st}), wherein the initial *Q*_{st} value of C₂H₆ for ZJU-HOF-1 (31.5 kJ mol⁻¹) is much higher than the 22.8 kJ mol⁻¹ observed in HOF-76a (Figure S21). Further, we also investigated the time-dependent ads/desorption kinetics profiles of ZJU-HOF-1 at 298 K. As shown in Figure S23, ZJU-HOF-1 exhibits similar adsorption kinetics for C₂H₆ and C₂H₄ with fast diffusion rates and the adsorbed molecules can be completely removed under

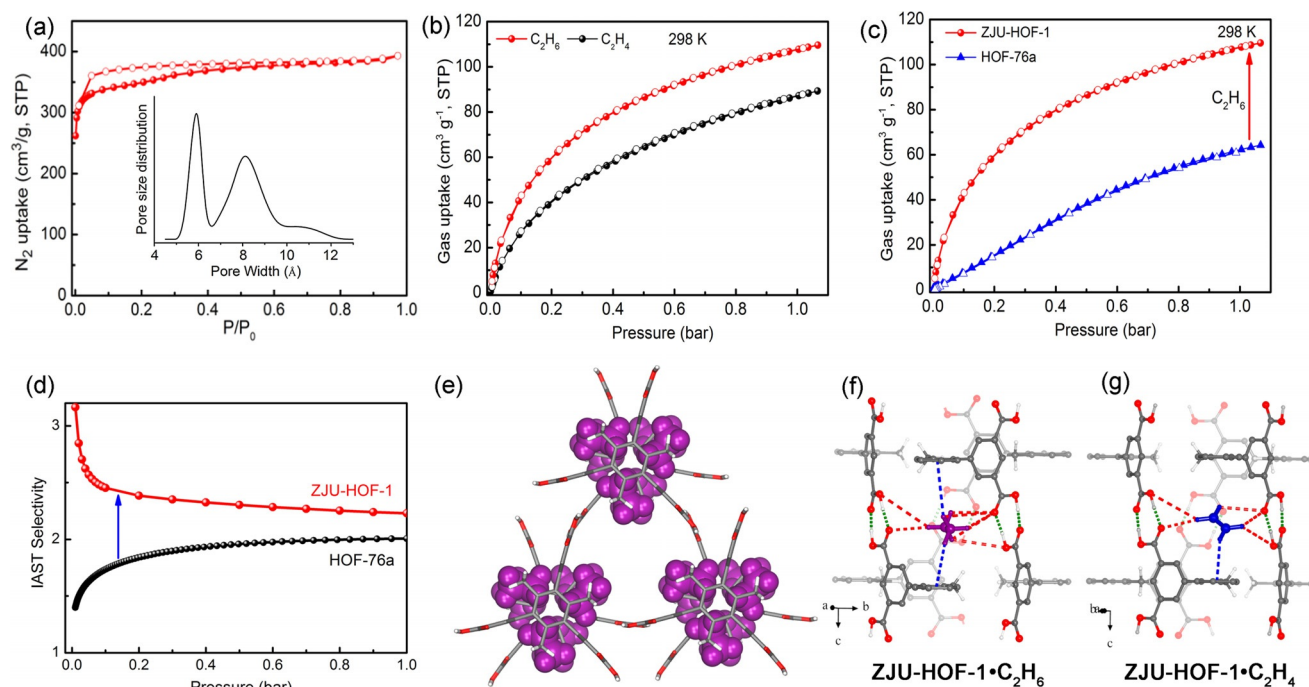


Figure 3. a) N₂ adsorption isotherms of ZJU-HOF-1 at 77 K. Inset shows pore size distribution for ZJU-HOF-1. b) Adsorption isotherms of C₂H₆ and C₂H₄ for ZJU-HOF-1 at 298 K. c) Comparison of C₂H₆ adsorption isotherms for ZJU-HOF-1 and HOF-76a at 298 K. d) C₂H₆/C₂H₄ IAST selectivity of ZJU-HOF-1 as compared with HOF-76a at 298 K. e) The C₂H₆ location observed by DFT calculations. f) Comparison of each pore cavity for the preferential C₂H₆ and g) C₂H₄ adsorption site (O, red; C, dark gray; H, white).

a high vacuum quickly, which are probably attributed to its comparably large pore channels.

Ideal adsorbed solution theory (IAST) was employed to estimate the adsorption selectivity of ZJU-HOF-1 for C_2H_6/C_2H_4 mixtures at 298 K. As indicated in Figure 3d, ZJU-HOF-1 exhibits a high C_2H_6/C_2H_4 selectivity of up to 3.2 at low pressure and 298 K for C_2H_6/C_2H_4 (50/50) mixtures. With the increase of pressure, it gradually decreases down to 2.25 at 1 bar. This value is notably higher than that of HOF-BTB (1.4) and HOF-76a (2.0).^[18] It is worth to note that high C_2H_6 uptake capacity is also very important to determine the C_2H_6/C_2H_4 separation performance. As shown in Figure S25, ZJU-HOF-1 exhibits an extremely high C_2H_6 uptake (3.2 mmol g⁻¹) from an equimolar mixture of C_2H_6/C_2H_4 as a function of IAST selectivity, far exceeding that of HOF-76a (1.62 mmol g⁻¹) and HOF-BTB (1.67 mmol g⁻¹). When we put gas uptake and selectivity as concurrent objectives, ZJU-HOF-1 shows a rare balance of both very high C_2H_6/C_2H_4 selectivity and C_2H_6 adsorption from C_2H_6/C_2H_4 mixtures, outperforming most of MOF materials reported (Figure S25).

To elucidate the origin of the observed high C_2H_6 uptake and selectivity, we performed detailed modeling studies using first-principles dispersion-corrected density functional theory (DFT-D) method on ZJU-HOF-1. We found that, for both C_2H_4 and C_2H_6 molecules, the primary adsorption sites are located at the small cage-like pockets within the corner of the triangular pore channels (Figure 3e). The lowest-energy gas binding sites are shown in Figure 3f,g. For clarity, we only showed one pocket site that can trap one gas molecule. Within each unit cell, there exist 6 such binding sites, which are crystallographically equivalent (Figure S26). The calculated

static binding energies for C_2H_6 and C_2H_4 are 34.4 and 31.7 kJ mol⁻¹, respectively. The stronger C_2H_6 -framework interactions are fully consistent with our experimental observations. This is partly because the nonplanar C_2H_6 molecule has more number of H atoms and sterically „matches“ better to the pocket size/shape than the planar C_2H_4 molecule. As a consequence, each C_2H_6 molecule interacts with two stacked phenyl rings and four oxygen atoms originated from four carboxylic groups to form two C-H... π interactions (H... π , 3.226 and 4.060 Å) and seven C-H...O interactions (H...O, 2.605–4.060 Å; Figure S27). In contrast, the C_2H_4 molecule shows only one C-H... π interaction with one phenyl ring (H... π , 3.212 Å) and five C-H...O interactions (H...O, 2.552–3.811 Å). Evidently, the higher binding energy of C_2H_6 can be mainly attributed to the suitable size and functional surfaces of the pockets that match better with C_2H_6 , thus leading to the more number of C-H... π and C-H...O interactions with the framework. A full occupancy of these binding sites would correspond to 4.91 mmol g⁻¹ gas uptake, which is very close to the experimental C_2H_6 uptake (4.82 mmol g⁻¹) at room temperature and 1 bar. In contrast, the much lower C_2H_4 uptake at room temperature and 1 bar suggests that only part of the binding sites are populated due to the weaker binding affinity with the framework. All of these results can explain the observed high C_2H_6 adsorption and separation performance at 1 bar qualitatively.

Transient breakthrough simulations were firstly conducted to preliminarily evaluate the feasibility of using ZJU-HOF-1 in a fixed bed for separation of C_2H_6/C_2H_4 (50/50 and 10/90) mixtures. As shown in Figure 4a, efficient separation

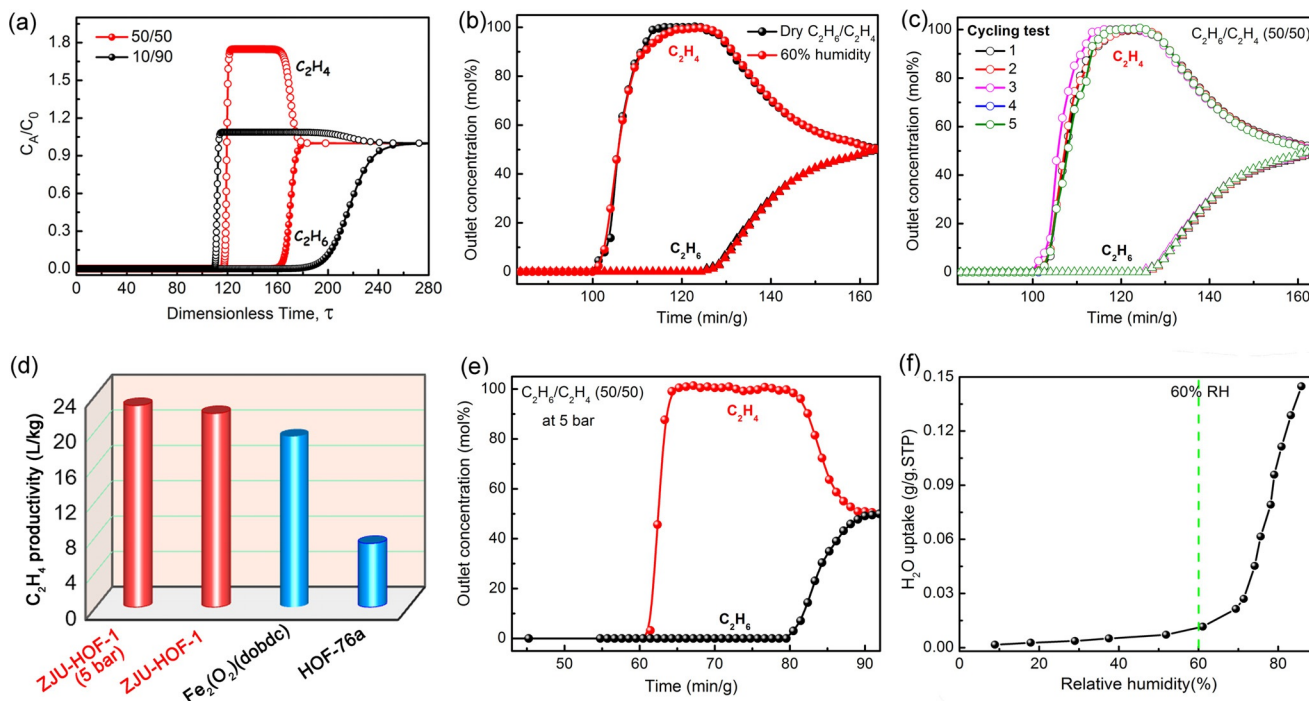


Figure 4. a) Simulated breakthrough curves for C_2H_6/C_2H_4 (50/50 and 10/90) separation (C_A/C_0 , outlet concentration/feed concentration). b) Experimental breakthrough curves for dry and wet C_2H_6/C_2H_4 (50/50) mixtures at 298 K and 1.01 bar. c) Recyclability of ZJU-HOF-1 in multiple mixed-gas column breakthrough tests. d) Comparison of C_2H_4 productivity in volume per unit mass of adsorbents. e) Experimental breakthrough curves for a 50/50 mixture at 298 K and 5 bar. f) Water vapor adsorption isotherm of ZJU-HOF-1 at 296 K.

can be realized by ZJU-HOF-1 for both 50/50 and 10/90 C₂H₆/C₂H₄ mixtures, wherein C₂H₄ breakthrough occurs first and then C₂H₆ passes through the fixed bed after a longer time (τ_{break}). Next, experimental breakthrough studies were performed in a packed column of ZJU-HOF-1 for actual C₂H₆/C₂H₄ (50/50 and 10/90) mixtures with a total flow of 1.25 mL min⁻¹ at 298 K. Figure 4c reveals that complete separation of C₂H₆ from C₂H₄ can be realized in ZJU-HOF-1. Ethylene was first eluted at 74 min to yield a pure gas with an undetectable amount of C₂H₆ (the detection limit of the instrument is 0.01 %), whereas the adsorbent retained C₂H₆ until 92 min. During this breakthrough process, pure C₂H₄ production (> 99.95 %) from the outlet effluent for a given cycle was calculated to be 0.98 mmol g⁻¹ (21.9 L kg⁻¹, Figure 4d), three times higher than HOF-76a (0.32 mmol g⁻¹ or 7.2 L kg⁻¹)^[18] and even outperforming that of the best MOF Fe₂(O₂)(dobdc) (0.86 mmol g⁻¹ or 19.3 L kg⁻¹).^[7a] The C₂H₄ productivity of ZJU-HOF-1 can be further improved to 1.02 mmol g⁻¹ at a high pressure of 5 bar (Figure 4e). It is worth to note that Fe₂(O₂)(dobdc) shows a high regeneration energy ($Q_{\text{st}} = 66.8 \text{ kJ mol}^{-1}$), and is not stable in air/moisture and requires harsh handling under inert conditions, which largely hampers its real-world applications. In strong contrast, ZJU-HOF-1 shows highly chemical stability and low regeneration energy (31.5 kJ mol⁻¹). This HOF can be easily regenerated to recover its separation capacity by the sweeping He gas at 323 K for 60 min, as evidenced by multiple breakthrough tests over five continuous cycles (Figure 4c).

In industrial C₂H₆/C₂H₄ separation, the feed gases typically contain water vapor, which could have negative effects on the uptake capacity and separation performance for many physisorbents. In this regard, many metal-containing materials such as MOFs and zeolites are sensitive to humidity or show high water uptake to result in competitive adsorption,^[25] thus suffering from gas sorption capacity reduction or structure decomposition under high humidity.^[7a,21a] To effectively avoid the effect of water vapor, ideal adsorbents would have not only high water stability but also low water uptake to minimize the co-adsorption of water. As shown in Figure 4f, thanks to the hydrophobic nature of HOFs,^[9a] we found that the water amount adsorbed in ZJU-HOF-1 is very low up to 60 % RH, with a negligible uptake of only 0.011 g g⁻¹. This could be highly favorable for C₂H₆/C₂H₄ separation under high humidity conditions. The breakthrough experiments on a wet C₂H₆/C₂H₄ mixture with 60 % humidity confirm that the presence of water vapor has no effect on the separation capacity of ZJU-HOF-1 (Figure 4b), further rendering it an ideal adsorbent for C₂H₄ purification under real industrial conditions.

Conclusion

In summary, we have realized the reversible solid-state transformation of a labile HOF material to result in a rod-packing desolvated structure (ZJU-HOF-1). This structural transition gives rise to the optimized pore confinement with suitable cavity spaces and functional surfaces in ZJU-HOF-1 for benchmark C₂H₆/C₂H₄ separation. The moderate high

surface area and unique pore architecture of ZJU-HOF-1 lead to a rare combination of both high C₂H₆ uptake capacity and excellent C₂H₆/C₂H₄ selectivity, both of which are higher than most of C₂H₆-selective materials. As revealed by DFT calculations, the suitable cage-like cavities and functional surfaces have collaborative roles for the preferential binding of C₂H₆ over C₂H₄. On account of the remarkable uptake and excellent selectivity, ZJU-HOF-1 exhibits the record polymer-grade C₂H₄ productivity of 0.98 mmol g⁻¹ (or 21.9 L kg⁻¹) from 50/50 dry and humid (60 % RH) C₂H₆/C₂H₄ mixtures at ambient conditions, even higher than the state-of-the-art Fe₂(O₂)(dobdc) reported so far. Combined with its extraordinary chemical stability and ultralow water uptake at high humidity, ZJU-HOF-1 embodies a new benchmark material that has the potential to be applied for C₂H₆/C₂H₄ separation in real-world applications. This work here not only reports the benchmark HOF material for C₂H₆/C₂H₄ separation, but also provides some guidance to design new porous HOFs with suitable pore confinement to address some other important and challenging gas separations.

Acknowledgements

This research was supported by the National Science Foundation of China (52073251 and 51803179) and the „Zhejiang University 100 Talent Program“.

Conflict of interest

The authors declare no conflict of interest.

Stichwörter: ethane capture · ethylene purification · gas separation · hydrogen bonds · microporous materials

- [1] H. A. Wittcoff, B. G. Reuben, J. S. Plotkin, *Industrial Organic Chemicals*, 2nd ed., Wiley, Hoboken, **2004**.
- [2] A. Corma, E. Corresa, Y. Mathieu, L. Sauvanaud, S. Al-Bogami, M. S. Al-Ghrami, A. Bourane, *Catal. Sci. Technol.* **2017**, *7*, 12–46.
- [3] D. S. Sholl, R. P. Lively, *Nature* **2016**, *532*, 435–437.
- [4] E. Worrell, D. Philipsen, D. Einstein, N. Martin, *Energy Use and Energy Intensity of the U. S. Chemical Industry*, Lawrence Berkeley National Laboratory, Berkeley, **2000**.
- [5] J. R. Li, J. Sculley, H. C. Zhou, *Chem. Rev.* **2012**, *112*, 869–932.
- [6] a) E. D. Bloch, W. L. Queen, R. Krishna, J. M. Zadrozny, C. M. Brown, J. R. Long, *Science* **2012**, *335*, 1606–1610; b) B. Li, Y. Zhang, R. Krishna, K. Yao, Y. Han, Z. Wu, D. Ma, Z. Shi, T. Pham, B. Space, J. Liu, P. K. Thallapally, J. Liu, M. Chrzanowski, S. Ma, *J. Am. Chem. Soc.* **2014**, *136*, 8654–8660.
- [7] a) L. Li, R.-B. Lin, R. Krishna, H. Li, S. Xiang, H. Wu, J. Li, W. Zhou, B. Chen, *Science* **2018**, *362*, 443–446; b) P.-Q. Liao, W.-X. Zhang, J.-P. Zhang, X.-M. Chen, *Nat. Commun.* **2015**, *6*, 8697; c) O. T. Qazvini, R. Babarao, Z.-L. Shi, Y.-B. Zhang, S. G. Telfer, *J. Am. Chem. Soc.* **2019**, *141*, 5014–5020; d) J. Pires, J. Fernandes, K. Dedecker, J. R. B. Gomes, G. Pérez-Sánchez, F. Nouar, C. Serre, M. L. Pinto, *ACS Appl. Mater. Interfaces* **2019**, *11*, 27410–27421; e) X. Wang, Z. Niu, A. M. Al-Enizi, A.

- Nafady, Y. Wu, B. Aguila, G. Verma, L. Wojtas, Y.-S. Chen, Z. Li, S. Ma, *J. Mater. Chem. A* **2019**, *7*, 13585–13590.
- [8] R. T. Yang, *Adsorbents: Fundamentals and Applications*, Wiley, Hoboken **2003**.
- [9] a) R.-B. Lin, Y. He, P. Li, H. Wang, W. Zhou, B. Chen, *Chem. Soc. Rev.* **2019**, *48*, 1362–1389; b) I. Hisaki, C. Xin, K. Takahashi, T. Nakamura, *Angew. Chem. Int. Ed.* **2019**, *58*, 11160–11170; *Angew. Chem.* **2019**, *131*, 11278–11288.
- [10] B. Wang, R.-B. Lin, Z. Zhang, S. Xiang, B. Chen, *J. Am. Chem. Soc.* **2020**, *142*, 14399–14416.
- [11] a) M. Mastalerz, I. M. Oppel, *Angew. Chem. Int. Ed.* **2012**, *51*, 5252–5255; *Angew. Chem.* **2012**, *124*, 5345–5348; b) A. Pulido, L. Chen, T. Kaczorowski, D. Holden, M. A. Little, S. Y. Chong, B. J. Slater, D. P. McMahon, B. Bonillo, C. J. Stackhouse, A. Stephenson, C. M. Kane, R. Clowes, T. Hasell, A. I. Cooper, G. M. Day, *Nature* **2017**, *543*, 657–664.
- [12] a) Q. Yin, P. Zhao, R.-J. Sa, G.-C. Chen, J. Lü, T.-F. Liu, R. Cao, *Angew. Chem. Int. Ed.* **2018**, *57*, 7691–7696; *Angew. Chem.* **2018**, *130*, 7817–7822; b) P. Li, P. Li, M. R. Ryder, Z. Liu, C. L. Stern, O. K. Farha, J. F. Stoddart, *Angew. Chem. Int. Ed.* **2019**, *58*, 1664–1669; *Angew. Chem.* **2019**, *131*, 1678–1683; c) P. Cui, E. S. Grape, P. R. Spackman, Y. Wu, R. Clowes, G. M. Day, A. K. Inge, M. A. Little, A. I. Cooper, *J. Am. Chem. Soc.* **2020**, *142*, 12743–12750; d) B. Wang, R. He, L.-H. Xie, Z.-J. Lin, X. Zhang, J. Wang, H. Huang, Z. Zhang, K. S. Schanze, J. Zhang, S. Xiang, B. Chen, *J. Am. Chem. Soc.* **2020**, *142*, 12478–12485.
- [13] a) K. Ma, P. Li, J. H. Xin, Y. Chen, Z. Chen, S. Goswami, X. Liu, S. Kato, H. Chen, X. Zhang, J. Bai, M. C. Wasson, R. R. Maldonado, R. Q. Snurr, O. K. Farha, *Cell Rep. Phys. Sci.* **2020**, *1*, 100024; b) I. Hisaki, S. Nakagawa, N. Ikenaka, Y. Imamura, M. Katouda, M. Tashiro, H. Tsuchida, T. Ogoshi, H. Sato, N. Tohnai, M. Miyata, *J. Am. Chem. Soc.* **2016**, *138*, 6617–6628; c) Y. Zhou, L. Kan, J. F. Eubank, G. Li, L. Zhang, Y. Liu, *Chem. Sci.* **2019**, *10*, 6565–6571; d) T. Takeda, M. Ozawa, T. Akutagawa, *Angew. Chem. Int. Ed.* **2019**, *58*, 10345–10352; *Angew. Chem.* **2019**, *131*, 10453–10460.
- [14] a) W. Liang, F. Carraro, M. B. Solomon, S. G. Bell, H. Amenitsch, C. J. Sumby, N. G. White, P. Falcaro, C. J. Doonan, *J. Am. Chem. Soc.* **2019**, *141*, 14298–14305; b) H. Yamagishi, H. Sato, A. Hori, Y. Sato, R. Matsuda, K. Kato, T. Aida, *Science* **2018**, *361*, 1242–1246; c) A. Karmakar, R. Illathvalappil, B. Anothumakkool, A. Sen, P. Samanta, A. V. Desai, S. Kurungot, S. K. Ghosh, *Angew. Chem. Int. Ed.* **2016**, *55*, 10667–10671; *Angew. Chem.* **2016**, *128*, 10825–10829.
- [15] a) Y. He, S. Xiang, B. Chen, *J. Am. Chem. Soc.* **2011**, *133*, 14570–14573; b) W. Yang, A. Greenaway, X. Lin, R. Matsuda, A. J. Blake, C. Wilson, W. Lewis, P. Hubberstey, S. Kitagawa, N. R. Champness, M. Schröder, *J. Am. Chem. Soc.* **2010**, *132*, 14457–14469.
- [16] a) X.-Z. Luo, X.-J. Jia, J.-H. Deng, J.-L. Zhong, H.-J. Liu, K.-J. Wang, D.-C. Zhong, *J. Am. Chem. Soc.* **2013**, *135*, 11684–11687; b) F. Hu, C. Liu, M. Wu, J. Pang, F. Jiang, D. Yuan, M. Hong, *Angew. Chem. Int. Ed.* **2017**, *56*, 2101–2104; *Angew. Chem.* **2017**, *129*, 2133–2136; c) I. Bassanetti, S. Bracco, A. Comotti, M. Negroni, C. Bezuidenhout, S. Canossa, P. P. Mazzeo, L. Marchiò, P. Sozzani, *J. Mater. Chem. A* **2018**, *6*, 14231–14239.
- [17] a) J. Lü, C. Perez-Krap, M. Suetin, N. H. Alsmail, Y. Yan, S. Yang, W. Lewis, E. Bichoutskaia, C. C. Tang, A. J. Blake, R. Cao, M. Schröder, *J. Am. Chem. Soc.* **2014**, *136*, 12828–12831; b) H. Wang, B. Li, H. Wu, T.-L. Hu, Z. Yao, W. Zhou, S. Xiang, B. Chen, *J. Am. Chem. Soc.* **2015**, *137*, 9963–9970; c) T.-H. Chen, I. Popov, W. Kaveevivitchai, Y.-C. Chuang, Y.-S. Chen, O. Daugulis, A. J. Jacobson, O. Š. Miljanić, *Nat. Commun.* **2014**, *5*, 5131–5139.
- [18] X. Zhang, L. Li, J.-X. Wang, H.-M. Wen, R. Krishna, H. Wu, W. Zhou, Z.-N. Chen, B. Li, G. Qian, B. Chen, *J. Am. Chem. Soc.* **2020**, *142*, 633–640.
- [19] a) Z. Bao, D. Xie, G. Chang, H. Wu, L. Li, W. Zhou, H. Wang, Z. Zhang, H. Xing, Q. Yang, M. J. Zaworotko, Q. Ren, B. Chen, *J. Am. Chem. Soc.* **2018**, *140*, 4596–4603; b) P. Li, Y. He, Y. Zhao, L. Weng, H. Wang, R. Krishna, H. Wu, W. Zhou, M. O’Keeffe, Y. Han, B. Chen, *Angew. Chem. Int. Ed.* **2015**, *54*, 574–577; *Angew. Chem.* **2015**, *127*, 584–587.
- [20] a) T.-U. Yoon, S. B. Baek, D. Kim, E.-J. Kim, W.-G. Lee, B. K. Singh, M. S. Lah, Y.-S. Bae, K. S. Kim, *Chem. Commun.* **2018**, *54*, 9360–9363; b) P. Li, Y. He, H. D. Arman, R. Krishna, H. Wang, L. Weng, B. Chen, *Chem. Commun.* **2014**, *50*, 13081–13084.
- [21] a) H. Zeng, X.-J. Xie, M. Xie, Y.-L. Huang, D. Luo, T. Wang, Y. Zhao, W. Lu, D. Li, *J. Am. Chem. Soc.* **2019**, *141*, 20390–20396; b) H. Yang, Y. Wang, R. Krishna, X. Jia, Y. Wang, A. N. Hong, C. Dang, H. E. Castillo, X. Bu, P. Feng, *J. Am. Chem. Soc.* **2020**, *142*, 2222–2227.
- [22] a) A. Cadiau, K. Adil, P. M. Bhatt, Y. Belmabkhout, M. Eddaoudi, *Science* **2016**, *353*, 137–140; b) H. Wang, X. Dong, V. Colombo, Q. Wang, Y. Liu, W. Liu, X.-L. Wang, X.-Y. Huang, D. M. Proserpio, A. Sironi, Y. Han, J. Li, *Adv. Mater.* **2018**, *30*, 1805088.
- [23] a) P. Nugent, Y. Belmabkhout, S. D. Burd, A. J. Cairns, R. Luebke, K. Forrest, T. Pham, S. Ma, B. Space, L. Wojtas, M. Eddaoudi, M. J. Zaworotko, *Nature* **2013**, *495*, 80–84; b) L. Jiang, Y. Tian, T. Sun, Y. Zhu, H. Ren, X. Zou, Y. Ma, K. R. Meihaus, J. R. Long, G. Zhu, *J. Am. Chem. Soc.* **2018**, *140*, 15724–15730.
- [24] a) L. Li, H.-M. Wen, C. He, R.-B. Lin, R. Krishna, H. Wu, W. Zhou, J. Li, B. Li, B. Chen, *Angew. Chem. Int. Ed.* **2018**, *57*, 15183–15188; *Angew. Chem.* **2018**, *130*, 15403–15408; b) H.-M. Wen, L. Li, R.-B. Lin, B. Li, B. Hu, W. Zhou, J. Hu, B. Chen, *J. Mater. Chem. A* **2018**, *6*, 6931–6937.
- [25] M. J. Kalmutzki, C. S. Diercks, O. M. Yaghi, *Adv. Mater.* **2018**, *30*, 1704304.

Manuskript erhalten: 8. Januar 2021

Akzeptierte Fassung online: 25. Februar 2021

Endgültige Fassung online: 26. März 2021

Supporting Information

A Rod-Packing Hydrogen-Bonded Organic Framework with Suitable Pore Confinement for Benchmark Ethane/Ethylene Separation

Xu Zhang⁺, Jia-Xin Wang⁺, Libo Li, Jiyan Pei, Rajamani Krishna, Hui Wu, Wei Zhou, Guodong Qian, Banglin Chen, and Bin Li**

ange_202100342_sm_miscellaneous_information.pdf

Supporting Information

1. General materials and procedures

All starting chemicals and solvents were purchased from commercial companies and used without further purification: 1,3,5-tribromo-2,4,6-trimethylbenzene (Adamas, 98+%), diethyl 5-bromo-1,3-benzenedicarboxylate was prepared from 5-bromoisophthalic acid (TCI, 98+%) according to the literature,^[1] bis(pinacol)diborane (Aladdin, 98%), Pd(PPh₃)₂Cl₂ (Aladdin, 98+%), Pd(PPh₃)₄ (Alfa Aesar, 99%), CuI (Acros, 98%). ¹H and ¹³C NMR spectra were recorded on Bruker AVANCE III spectrometers (400 MHz). Thermogravimetric analyses (TGA) were performed on a Netzsch STA 449C thermal analyzer from 30 to 800 °C under nitrogen atmosphere at a heating rate of 5 °C/minute rate. Powder X-ray diffraction (PXRD) patterns were measured by a BRUKER D8 ADVANCE diffractometer employing Cu-K_α radiation operated at 30 kV and 15 mA, scanning over the range 2-45° (2θ) at a rate of 2°/min.

C₂H₄ (99.99%), C₂H₆ (99.99%), He (99.999%) and mixed gases of C₂H₄/C₂H₆ = 10/90 (v/v), and C₂H₄/C₂H₆ = 50/50 (v/v) mixtures were purchased from Beijing Special Gas Co. LTD (China).

2. Single-crystal X-ray crystallography

Single-crystal X-ray diffraction data of the as-synthesized crystal was collected on a Bruker D8 VENTURE diffractometer at 100 K using graphite-monochromated Mo-K_α ($\lambda = 0.71073 \text{ \AA}$) radiation. The structure was solved by direct method and refined on F^2 by full-matrix least-squares methods using SHELXL-97 software package.^[2] The solvate molecules were treated as diffuse contribution to the overall scattering without specific atom positions by SQUEEZE/PLATON due to severe disorder of these solvate molecules in the lattices. The crystal data are summarized in Table S2 (Supporting Information).

3. Powder X-ray crystallography

Attempts to obtain single-crystal structure of activated ZJU-HOF-1 were not successful because the large stick-like as-synthesized crystals would crack into smaller crystals upon evacuation (Figure S9 and S16). We thus relied on powder X-ray diffraction (PXRD) to simulate

the crystallographic structure of ZJU-HOF-1.^[3,4] The PXRD measurements were performed on a Rigaku Ultima IV diffractometer, operated at 40 kV and 44 mA and CuK α radiation ($\lambda = 1.5406$ Å). Data were collected at room temperature in the 2θ range of 2–45° with a step size of 1.0°. We reason that since the HOF structural change is fully reversible upon desolvation/re-solvation, the overall HOF network connection must remain largely the same. Based on the powder pattern indexing, we first figured out and identified the new crystal symmetry of a hexagonal $P-6c2$ space group for the activated phase. With the symmetry known and the overall network connection known, a model was constructed straightforwardly in computer. We then further optimized the structure based on DFT calculations. We did attempt Rietveld structural refinement on the PXRD pattern, but we found the refinement rather difficult to converge, because of the following two reasons: 1) the relatively large dimension of the HOF unit cell and the relatively large number of independent atoms within the unit cell, and 2) the limited number of diffraction peaks in the Lab PXRD pattern. Fortunately, as shown in Figure S10, the simulated PXRD pattern of our structural model agrees excellently with the experimental data, which strongly supports its validity. Unit cell parameters of ZJU-HOF-1 from peak fitting are $a = b = 12.6754$ Å, $c = 16.8735$ Å; $\alpha = \beta = 90.00$, $\gamma = 120.00$, which are different with those of as-synthesized JLU-SOF3 crystal. Detailed structure information of ZJU-HOF-1 is provided in Tables S3 and S4, and the model cif file of ZJU-HOF-1 is supplied as a separated SI file.

4. Gas Sorption Measurements. A Micromeritics ASAP 2020 surface area analyzer was used to measure gas adsorption isotherms. To remove all the guest solvents in the framework, the fresh powder samples were first solvent-exchanged with dry ethyl ether at least 10 times within two days, and evacuated at room temperature for 48 h and then at 323 K for 12 h until the outgas rate was 5 mmHg min⁻¹ prior to measurements. The sorption measurement was maintained at 77 K under liquid nitrogen bath. Julabo water bath was used to keep the adsorption tube at a constant temperature of 273 and 298 K, respectively. The water adsorption isotherms were measured at the Belsorp-Max II instrument.

Kinetic and equilibrium adsorption were measured with the Intelligent Gravimetric Analyzer (IGA001, Hiden, UK), which uses a gravimetric technique to accurately measure the gas sorption on porous materials under diverse operating conditions. About 50 mg ZJU-HOF-1 sample was loaded into the sample cell, and then the system was outgassed prior to gas sorption measurements. All the gases used (C_2H_4 , C_2H_6 , and He) were of 99.99% purity.

5. Fitting of pure component isotherms

The pure component isotherm data for C_2H_4 and C_2H_6 in ZJU-HOF-1 were measured at 273 K and 298 K. The data were fitted with the dual-Langmuir-Freundlich isotherm model

$$q = q_{A,sat} \frac{b_A p^{v_A}}{1 + b_A p^{v_A}} + q_{B,sat} \frac{b_B p^{v_B}}{1 + b_B p^{v_B}}$$

with T -dependent parameters b_A , and b_B

$$b_A = b_{A0} \exp\left(\frac{E_A}{RT}\right); \quad b_B = b_{B0} \exp\left(\frac{E_B}{RT}\right)$$

The fitted parameter values are provided in Table S1 and Figure S22.

6. Virial Graph Analysis

Estimation of the isosteric heats of gas adsorption (Q_{st})

A virial-type expression of comprising the temperature-independent parameters a_i and b_j was employed to calculate the enthalpies of adsorption for C_2H_6 and C_2H_4 (at 273 K and 298 K) on ZJU-HOF-1. In each case, the data were fitted use equation:

$$\ln P = \ln N + 1/T \sum_{i=0}^m a_i N_i + \sum_{j=0}^n b_j N_j$$

Here, P is the pressure expressed in mmHg, N is the amount absorbed in mmol g^{-1} , T is the temperature in K, a_i and b_j are virial coefficients, and m , n represent the number of coefficients required to adequately describe the isotherms (m and n were gradually increased till the contribution of extra added a and b coefficients was deemed to be statistically insignificant towards the overall fit. And the average value of the squared deviations from the experimental

values was minimized). The values of the virial coefficients a_0 through a_m were then used to calculate the isosteric heat of adsorption using the following expression:

$$Q_{st} = -R \sum_{i=0}^m a_i N_i$$

Q_{st} is the coverage-dependent isosteric heat of adsorption and R is the universal gas constant. The heat enthalpy of C_2H_6 and C_2H_4 sorption for ZJU-HOF-1 in this manuscript are determined by using the sorption data measured in the pressure range from 0-1 bar (at 273 K and 298 K). The Q_{st} values as function of the molar loadings are provided in Figure S21.

7. IAST calculations of adsorption selectivities

The selectivity of preferential adsorption of component 1 (C_2H_6) over component 2 (C_2H_4) can be defined as

$$S_{ads} = \frac{q_1/q_2}{p_1/p_2}$$

Where q_1 and q_2 are the *absolute* component loadings of the adsorbed phase in the mixture, and p_1 and p_2 are the component partial pressures. The component loadings and adsorption selectivity S_{ads} for 50/50 $C_2H_6(1)/C_2H_4(2)$ mixtures in ZJU-HOF-1 at 298 K were determined using IAST.

8. Density-functional theory calculations

The First-principles density-functional theory (DFT) calculations were performed using the Quantum-Espresso package.^[5] A semi-empirical addition of dispersive forces to conventional DFT^[5] was included in the calculation to account for van der Waals interactions. We used Vanderbilt-type ultrasoft pseudopotentials and the generalized gradient approximation (GGA) with the Perdew-Burke-Ernzerhof (PBE) exchange correlation. We first fully optimized the bare ZJU-HOF-1 structure, using the primitive unit cell. Then, C_2H_6 and C_2H_4 molecules were introduced into the pores of ZJU-HOF-1, and structural relaxations were performed. Various gas adsorption positions and molecular orientations were examined to find the lowest energy configuration. To obtain the gas binding energies, a single gas molecule placed in a supercell

with the same cell dimensions was also relaxed as a reference. The static binding energy (at $T = 0$ K) was calculated using: $E_B = E_{(\text{ZJU-HOF-1})} + E_{(\text{gas})} - E_{(\text{ZJU-HOF-1+gas})}$.

9. Breakthrough simulations

The performance of industrial fixed bed adsorbers is dictated by a combination of adsorption selectivity and uptake capacity. Transient breakthrough simulations were carried out for 50/50 $\text{C}_2\text{H}_6/\text{C}_2\text{H}_4$ and 10/90 $\text{C}_2\text{H}_6/\text{C}_2\text{H}_4$ mixtures in ZJU-HOF-1 operating at a total pressure of 100 kPa and 298 K, using the methodology described in earlier publications.^[7-10] For the breakthrough simulations, the following parameter values were used: length of packed bed, $L = 0.3$ m; voidage of packed bed, $\varepsilon = 0.4$; superficial gas velocity at inlet, $u = 0.04$ m/s.

The transient breakthrough simulation results are presented in terms of a dimensionless time, $\tau = \frac{tu}{L\varepsilon}$, defined by dividing the actual time, t , by the characteristic time, $\frac{L\varepsilon}{u}$. The y-axis is the dimensionless concentration of each species at the exit of the adsorber, c_A divided by the inlet concentrations of that species, c_{A0} .

The breakthrough simulations demonstrate the potential of producing product gas C_2H_4 of required purity during the interval $\Delta\tau$.

10. Column Breakthrough Experiments. The breakthrough experiments were performed in dynamic gas breakthrough equipment using a stainless steel column (4.0 mm inner diameter \times 150 mm). The weight of sample packed in the column was: 0.7403 g. The mixed gas flows of (1) dry and wet $\text{C}_2\text{H}_6/\text{C}_2\text{H}_4 = 50/50$ (v/v) and (2) $\text{C}_2\text{H}_6/\text{C}_2\text{H}_4 = 10/90$ (v/v) were then introduced at 1.25 mL min^{-1} . In addition, activated samples (2.1 g) were packed into $\Phi 4 \times 350$ mm stainless steel column for the breakthrough experiments under gas flow of 50/50 $\text{C}_2\text{H}_6/\text{C}_2\text{H}_4$ at 298 K and 5.0 bar. Outlet gas from the column was monitored using gas chromatography (GC-2014C, SHIMADZU) with a thermal conductivity detector (TCD, detection limit 0.1 ppm). The standard gases were used to calibrate the concentration of the outlet gas. After the breakthrough tests, ZJU-HOF-1a can be readily regenerated by sweeping He gas (10 mL min^{-1}) at 323 K for 60 min.

11. Structural transformation and stability studies

To investigate the possible structural transformation between JLU-SOF3 and the activated ZJU-HOF-1, the as-synthesized samples were treated by air exposure, heating or vacuum degassing, respectively. As revealed by PXRD patterns (Figure S12 and S13), the framework of JLU-SOF3 can gradually transfer to ZJU-HOF-1 with the removal of solvent molecules upon the above treatments. Subsequently, the ZJU-HOF-1 samples were immersed into Et₂O or H₂O solution, and the structure can be reversibly converted to JLU-SOF3 after the solvent molecules enter the pores, as indicated by the PXRD patterns (Figure S14). These results clearly indicate that the structure can be reversibly transformed between JLU-SOF3 and the activated ZJU-HOF-1 upon desolvation or solvation.

To example the chemical stabilities of ZJU-HOF-1, the as-synthesized samples were soaked in water, HCl (pH = 1) and NaOH (pH = 10) solutions for 2 days, respectively. After that, each sample was filtered and washed with water and acetone quickly, and then characterized by PXRD measurements in order to determine whether the sample retains its structural integrity. Subsequently, each sample was solvent-exchanged with dry acetone at least 8 times within two hours to completely remove the hardly volatile H₂O molecules in the pores, and then was activated by the activation conditions prior to gas sorption measurements. The 77 K N₂ sorption isotherms were examined to further determine the chemical stability of ZJU-HOF-1.

Notation

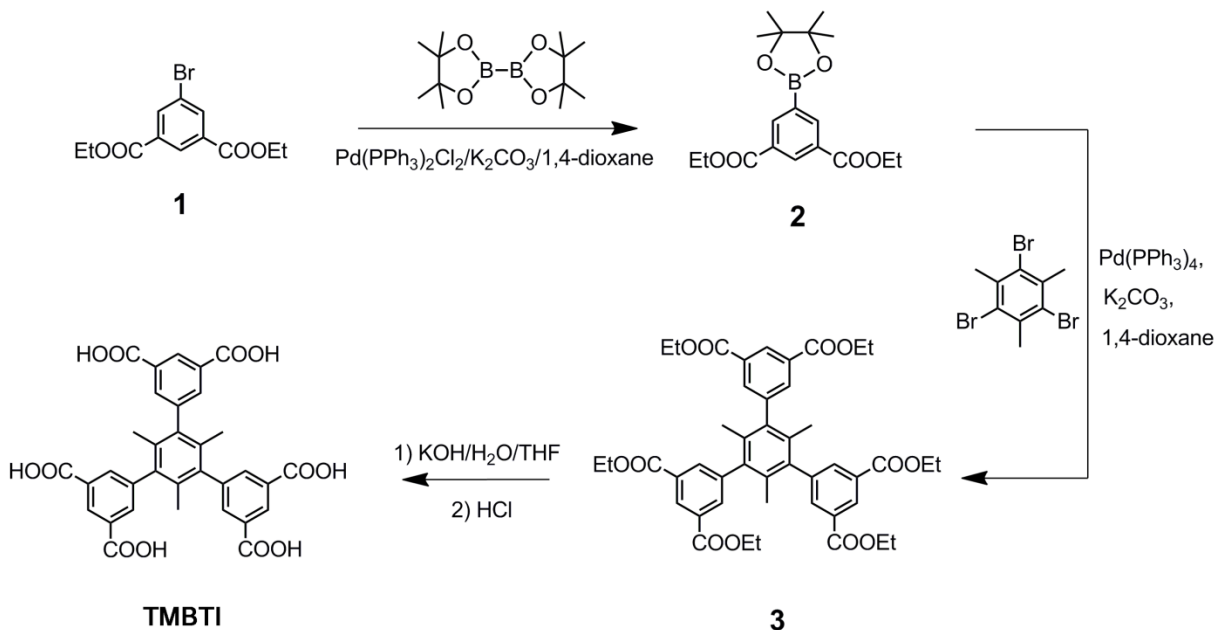
b_A	Langmuir-Freundlich constant for species i at adsorption site A, Pa ^{-V_{iA}}
b_B	Langmuir-Freundlich constant for species i at adsorption site B, Pa ^{-V_{iB}}
c_i	molar concentration of species i in gas mixture, mol m ⁻³
c_{i0}	molar concentration of species i in gas mixture at inlet to adsorber, mol m ⁻³
E	energy parameter, J mol ⁻¹
p_i	partial pressure of species i in mixture, Pa
p_t	total system pressure, Pa
q_i	component molar loading of species i , mol kg ⁻¹
Q_{st}	isosteric heat of adsorption, J mol ⁻¹

T	absolute temperature, K
L	length of packed bed adsorber, m
t	time, s
T	absolute temperature, K
u	superficial gas velocity in packed bed, m s^{-1}

Greek letters

ε	voidage of packed bed, dimensionless
ν	Freundlich exponent, dimensionless
τ	time, dimensionless

Scheme S1. Synthetic routes to the organic building block TMBTI.



Synthesis of diethyl 5-(4,4,5,5-tetramethyl-1,3,2-dioxaborolan-2-yl) isophthalate (2). Under an argon atmosphere, diethyl 5-bromo-1,3-benzenedicarboxylate (**1**) (3.0 g, 10.0 mmol), bis(pinacol)diborane (2.67 g, 10.5 mmol), Pd(PPh₃)₂Cl₂ (280 mg, 0.40 mmol), K₂CO₃ (2.76 g, 20.0 mmol), and fresh distilled dry 1,4-dioxane (100 mL) were combined in a 250 mL two neck round bottom flask. This mixture was stirred at refluxing temperature for 24 h. After removal of organic solvent, the crude product was purified by column chromatography on silica gel with petroleum ether/ethyl acetate (10:1 v/v) to give compound **2** as a white solid. Yield: 3.03 g, 87%. ¹H NMR (CDCl₃, 400 MHz): δ 8.75 (t, *J* = 1.76 Hz, 1H), 8.61 (d, *J* = 1.76 Hz, 2H), 4.41 (q, *J* = 7.13 Hz, 4H), 1.41 (t, *J* = 7.14 Hz, 6H), 1.36 (s, 12H). ¹³C NMR (CDCl₃, 100 MHz): δ 166.1, 139.9, 133.4, 130.5, 84.5, 61.4, 25.0, 14.5.

Synthesis of compound 3. Under an argon atmosphere, compound **2** (2.68 g, 9.8 mmol), 1,3,5-tribromo-2,4,6-trimethylbenzene (0.8 g, 2.2 mmol), Pd(PPh₃)₄ (230 mg, 0.20 mmol), K₂CO₃ (2.76 g, 20.0 mmol), and fresh distilled dry 1,4-dioxane (100 mL) were combined in a 250 mL two neck round bottom flask. This mixture was stirred at refluxing temperature for 48 h. After removal of organic solvent, the crude product was purified by column chromatography on silica gel with petroleum ether/ethyl acetate (4:1 v/v) to give compound **3** as a white solid. Yield: 1.44 g, 82%. ¹H NMR (CDCl₃, 400 MHz): δ 8.69 (t, *J* = 1.56 Hz, 3H), 8.10 (d, *J* = 1.64 Hz, 6H), 4.42

(q, $J = 7.12$ Hz, 12H), 1.67 (s, 9H), 1.43 (t, $J = 7.14$ Hz, 18H). ^{13}C NMR (CDCl_3 , 100 MHz): δ 165.9, 142.3, 138.5, 134.7, 133.8, 131.7, 129.4, 61.6, 19.9, 14.5.

Synthesis of 2,4,6-trimethylbenzene-1,3,5-triylisophthalate (TMBTI). Under an argon atmosphere, a solution of compound **3** (1.0 g, 1.28 mmol) in THF (60 mL) was added to a 60 mL water solution of KOH (3.36 g, 60 mmol). The mixture was stirred at 100 °C for 72 h. After removal of organic solvent, the aqueous residue was acidified with 2 M HCl. The resulting precipitate was filtered, washed with water, and dried under vacuum to afford **TMBTI** as a white solid. Yield: 738 mg, 94%. ^1H NMR ($\text{DMSO-}d_6$, 400 MHz): δ 13.36 (br, 6H), 8.48 (s, 3H), 8.01 (d, $J = 1.36$ Hz, 6H), 1.61 (s, 9H). ^{13}C NMR ($\text{DMSO-}d_6$, 100 MHz): δ 166.6, 141.8, 138.0, 134.1, 132.7, 132.0, 128.7, 19.4.

Synthesis of ZJU-HOF-1. The 100 mg TMBTI was dissolved in 20 mL of THF in a 50 mL beaker, which was put in a 250 mL sealed beaker with 100 mL ethyl ether. The colorless stick-like crystals suitable for single crystal X-ray diffraction analysis were grown by vapor diffusion for two weeks at room temperature. Yield: 93 mg, 93%. The as-synthesized sample can be desolvated in high vacuum at 323 K to generate the activated sample ZJU-HOF-1 with a new structure.

Table S1. Dual-Langmuir-Freundlich parameter fits for C₂H₆ and C₂H₄ in ZJU-HOF-1. The fits are based on experimental isotherm data at 298 K.

	Site A			Site B		
	$q_{A,sat}$ mol kg ⁻¹	b_{A0} kPa ^{-ν_A}	\square_A dimensionless	$q_{B,sat}$ mol kg ⁻¹	b_{B0} kPa ^{-ν_B}	\square_B dimensionless
C ₂ H ₆	3.03696	0.10845	0.82742	5.5357	0.02174	0.75476
C ₂ H ₄	1.09006	0.11965	1.05675	6.4095	0.01141	0.92543

Table S2. Crystallographic data and structure refinement results of as-synthesized crystal.

	JLU-SOF3
Empirical formula	C ₃₃ H ₂₄ O ₁₂
Formula weight	612.52
Crystal system	Hexagonal
Space group	<i>P</i> $\bar{6}$ 2 <i>c</i>
<i>a</i> (Å)	22.7034(16)
<i>b</i> (Å)	22.7034(16)
<i>c</i> (Å)	16.6845(11)
α (°)	90
β (°)	90
γ (°)	120
<i>V</i> (Å ³)	7447.8(12)
<i>Z</i>	6
ρ_{calcd} (g/cm ⁻³)	0.819
μ (mm ⁻¹)	0.063
Radiation (λ , Å)	0.71073
F(000)	1908.0
Temperature (K)	100(2)
Number of collected data	5677
Number of unique data	2749
Completeness	99.9
GOF	1.018
<i>RI</i> (<i>F</i> _o) ^a	0.0574
<i>wR2</i> (<i>F</i> _o ²) ^b	0.1799
CCDC number	1971951

^a $RI = \Sigma|F_o - F_c|/\Sigma F_o$, ^b $wR2 = \Sigma[w(F_o^2 - F_c^2)^2]/\Sigma[w(F_o^2)]^{1/2}$

Table S3. Lattice parameters of the modeled structure of activated ZJU-HOF-1.

ZJU-HOF-1	
Empirical formula	C ₃₃ H ₂₄ O ₁₂
Formula weight	612.52
Crystal system	Hexagonal
Space group	<i>P</i> $\bar{6}$ <i>c</i> 2
<i>a</i> (Å)	12.6754
<i>b</i> (Å)	12.6754
<i>c</i> (Å)	16.8735
α (°)	90
β (°)	90
γ (°)	120
<i>V</i> (Å ³)	2347.7
<i>Z</i>	2
ρ_{calcd} (g/cm ⁻³)	0.866

Table S4. List of atomic coordinates for the modeled structure of activated ZJU-HOF-1.

Atoms	x	y	z	s.o.f.
H1	0.53349	0.59708	0.37782	1.00
H2	0.83756	0.53503	0.45468	1.00
H3	0.31254	0.39212	0.30227	1.00
C4	0.70991	0.54658	0.39977	1.00
C5	0.66255	0.55797	0.32157	1.00
C6	0.56870	0.58626	0.32124	1.00
O7	0.66218	0.55469	0.46249	1.00
O8	0.80469	0.52946	0.39740	1.00
H9	0.78424	0.52351	0.25000	1.00
H10	0.17425	0.34782	0.25000	1.00
C11	0.52212	0.60222	0.25000	1.00
C12	0.71057	0.54433	0.25000	1.00
C13	0.42546	0.63639	0.25000	1.00
C14	0.30234	0.54265	0.25000	1.00
C15	0.27279	0.41149	0.25000	1.00

Table S5. Summary of separation metrics of ethane-selective HOF materials reported in the literature at 1 bar and room temperature (RT).

C ₂ H ₆ -selective adsorbents	C ₂ H ₆ uptake ^a (mmol/g)	Selectivity ^b	$Q_{st, \text{ethane}}$ (kJ/mol) ^c	Productivity _{exp} (L/kg) ^d	T (K)	Ref.
ZJU-HOF-1	3.93	2.25	31.5	21.9	298	This work
HOF-76a	1.69	2.05	22.8	7.2	296	[11]
HOF-BTB ^e	2.10	1.4	25.4	-	295	[12]

^a At 0.5 bar and RT; ^b IAST selectivity for 50/50 C₂H₆/C₂H₄ gas mixtures; ^c The adsorption heat (Q_{st}) of C₂H₆ at low surface coverage. ^d The pure C₂H₄ productivity calculated from breakthrough experiments at 1 bar and RT on 50/50 gas mixtures. ^e The reported literature only described the C₂H₄ and C₂H₆ adsorption isotherms, so the selectivity and uptake ratio were evaluated based on these isotherms.

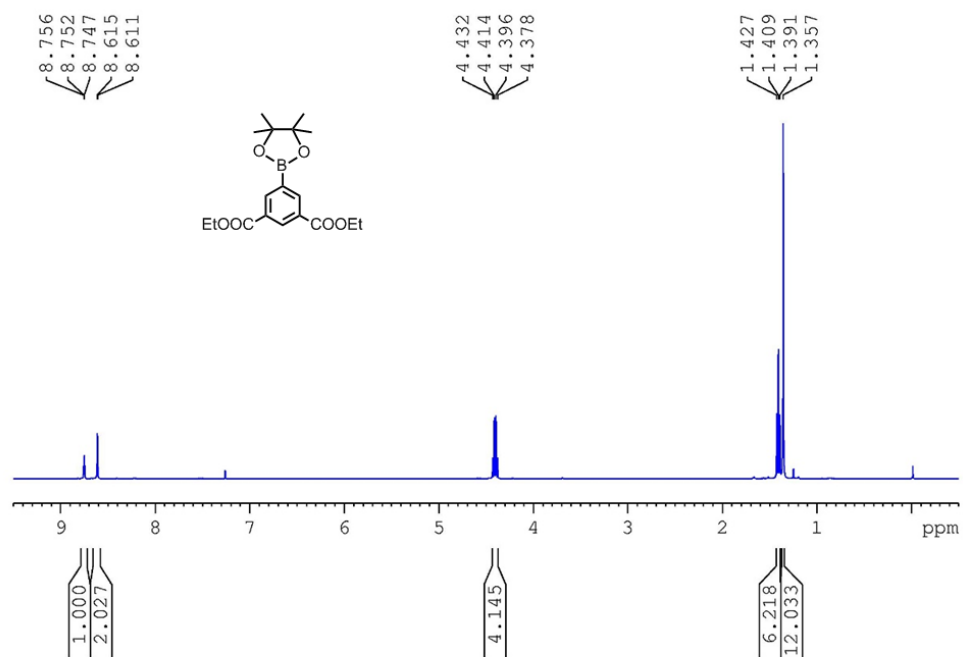


Figure S1. ¹H NMR (CDCl₃, 400 MHz) spectrum of compound **2**.

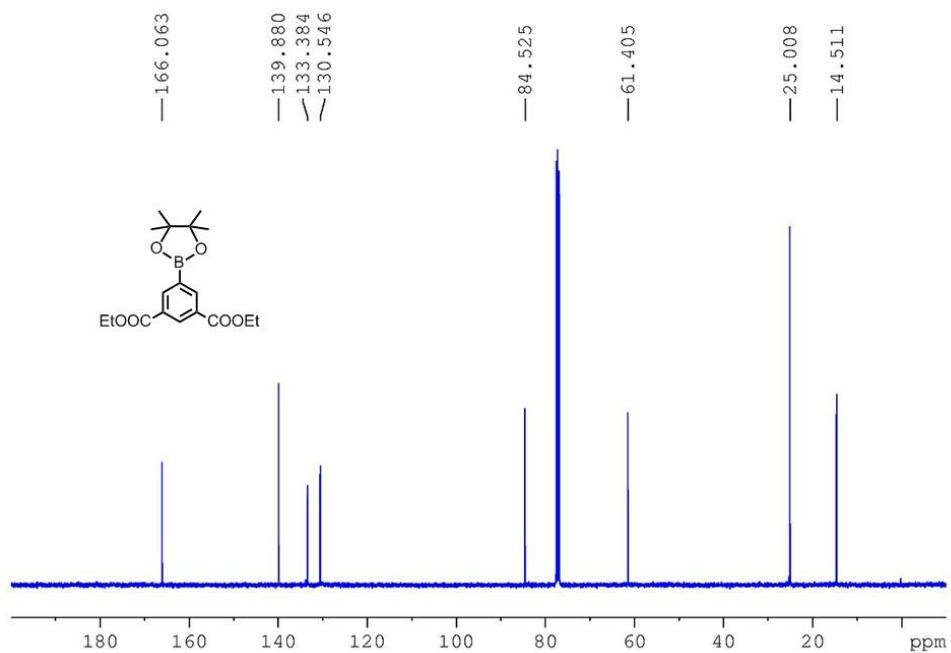


Figure S2. ¹³C NMR (CDCl₃, 100 MHz) spectrum of compound **2**.

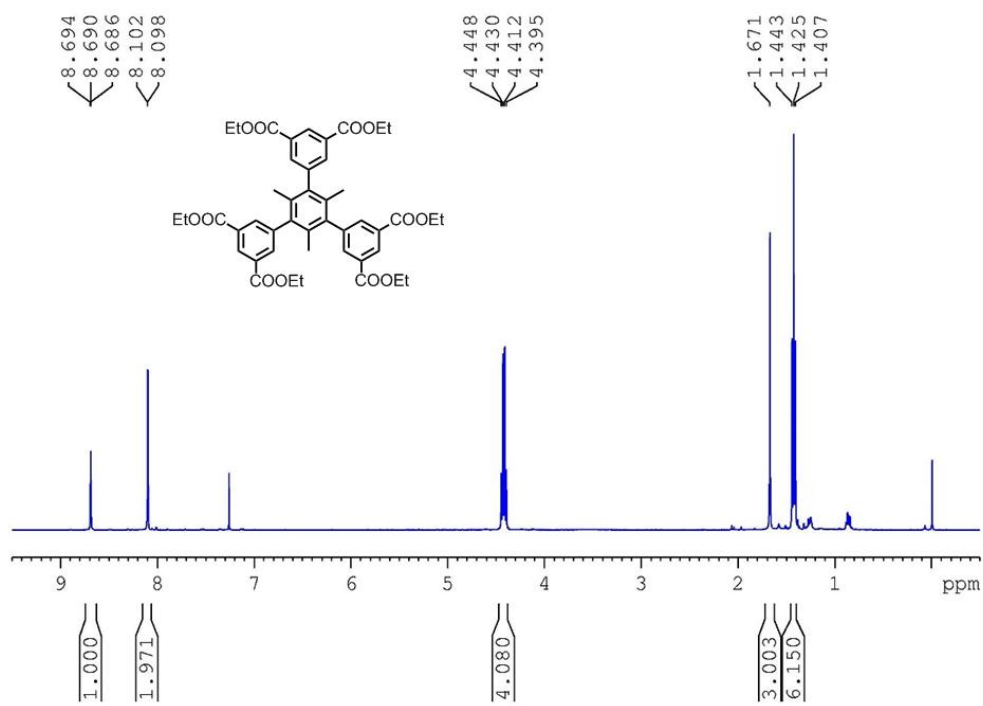


Figure S3. ¹H NMR (CDCl₃, 400 MHz) spectrum of compound **3**.

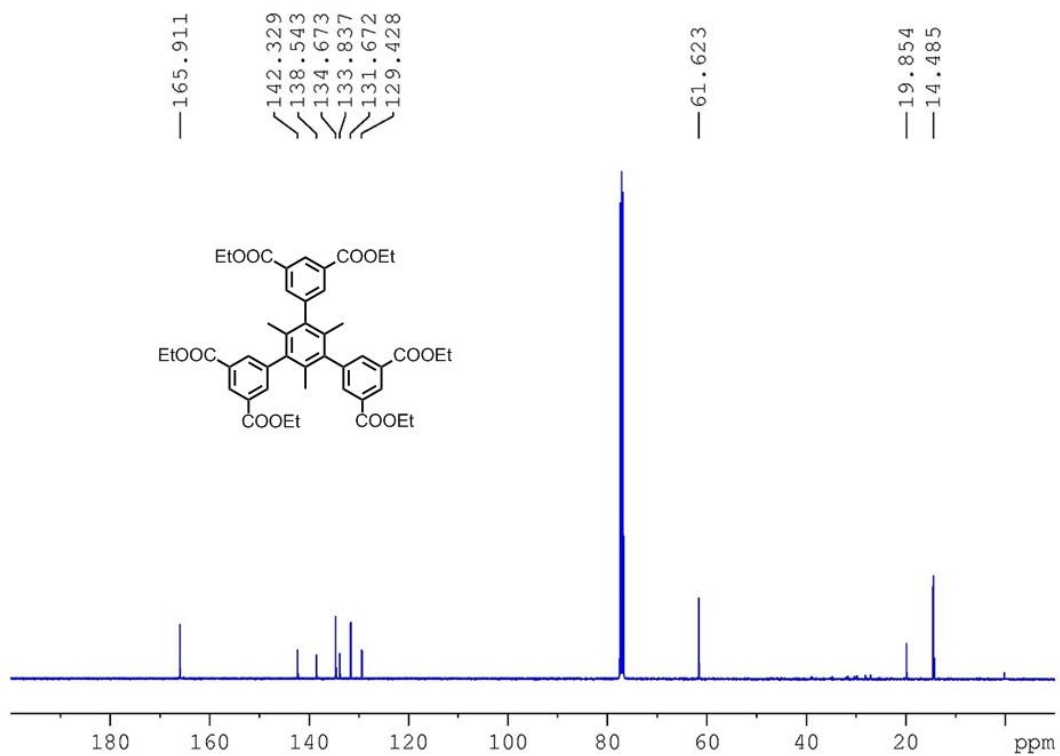


Figure S4. ¹³C NMR (CDCl₃, 100 MHz) spectrum of compound **3**.

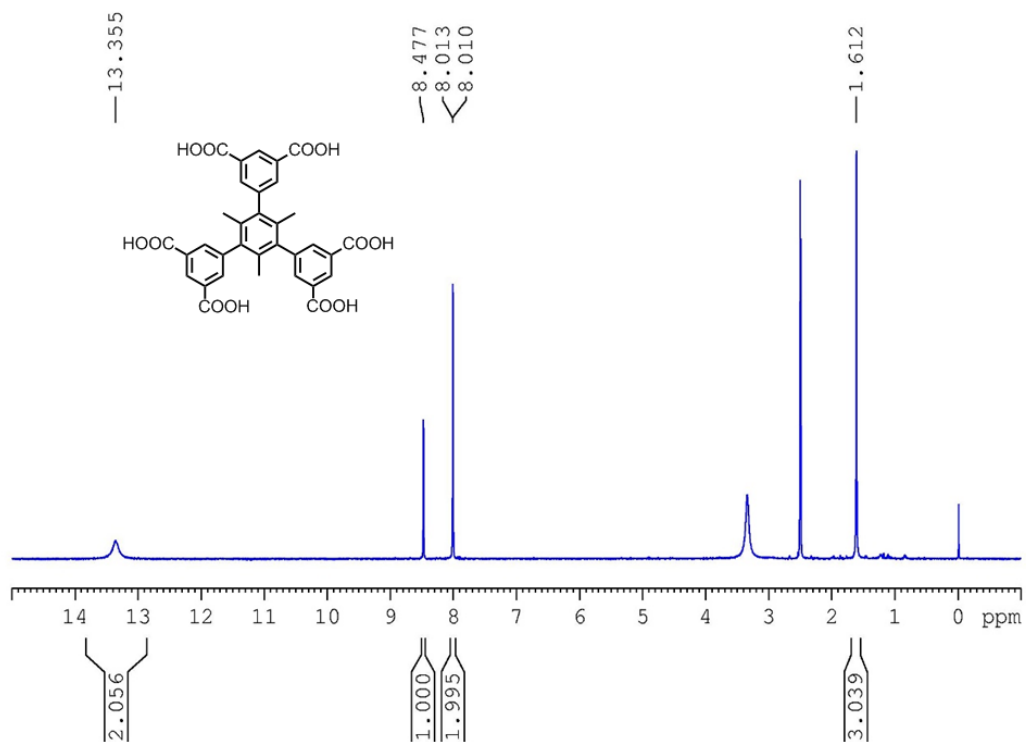


Figure S5. ^1H NMR (DMSO- d_6 , 400 MHz) spectrum of compound TMBTI.

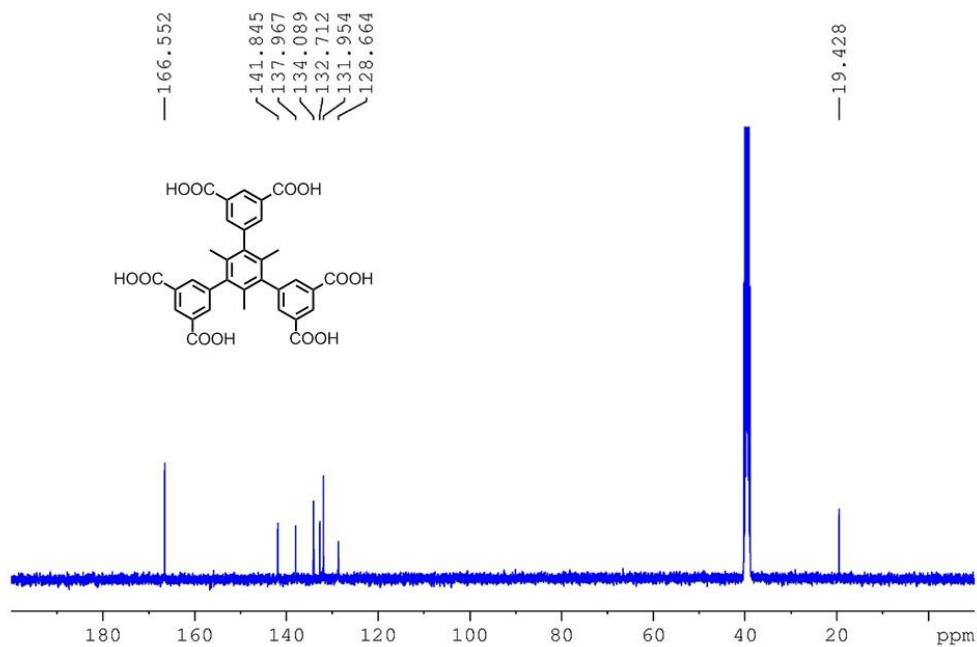


Figure S6. ^{13}C NMR (DMSO- d_6 , 100 MHz) spectrum of compound TMBTI.

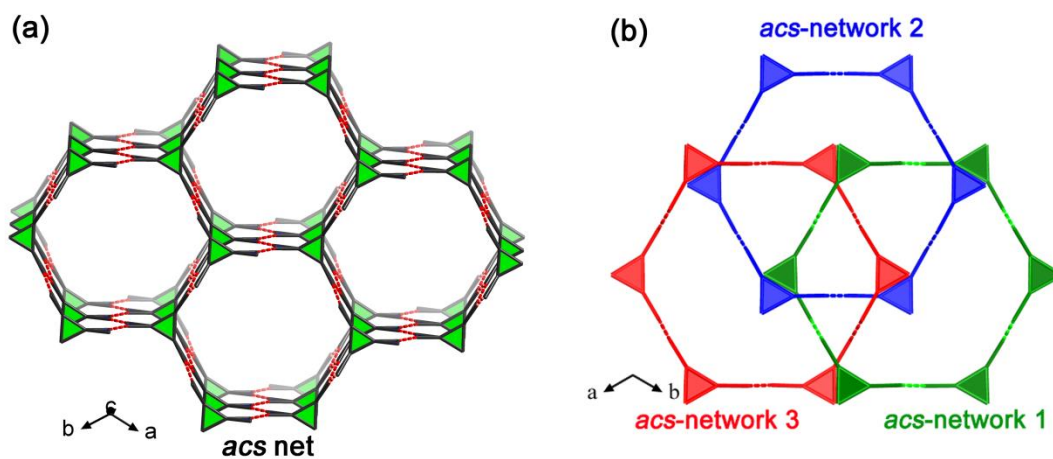


Figure S7. (a) Topology description of JLU-SOF3, showing the *acs*-network viewed along the *c* axis and (b) the 3-fold interpenetrated network.

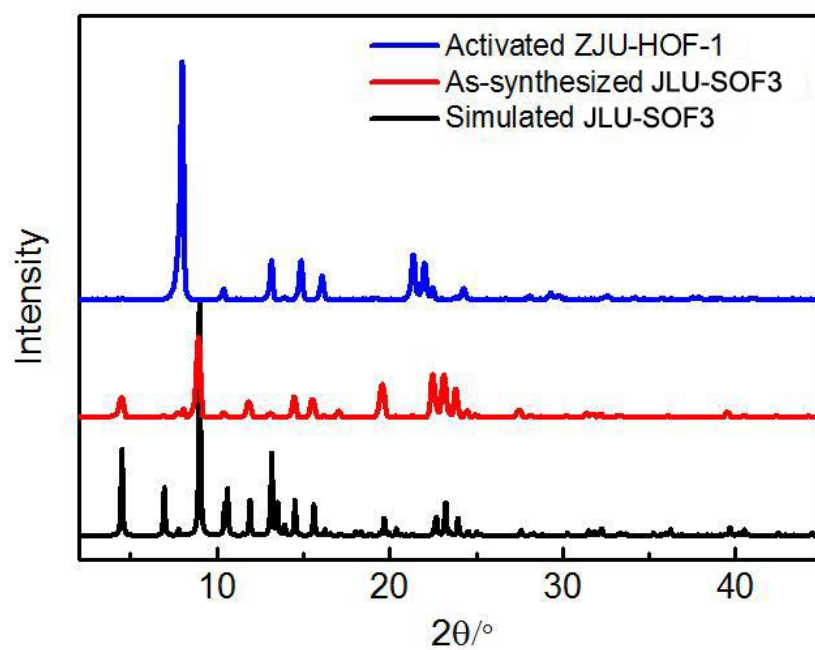


Figure S8. PXRD patterns of as-synthesized JLU-SOF3 (red) and activated ZJU-HOF-1 (blue) along with the simulated XRD pattern based on the crystal structure of JLU-SOF3 (black).

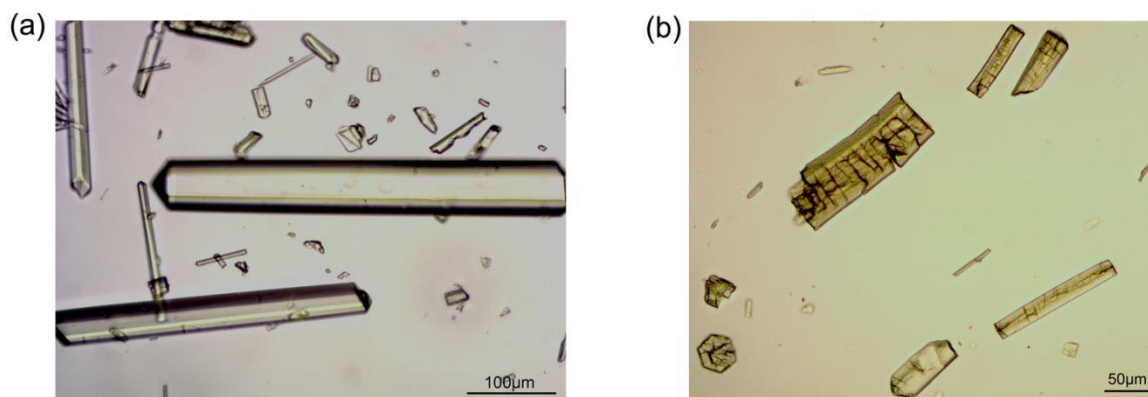


Figure S9. The optical photos of (a) the as-synthesized crystals and (b) activated ZJU-HOF-1 sample, indicating that the larger single-crystals would break into much smaller low-quality crystallites during the activation process.

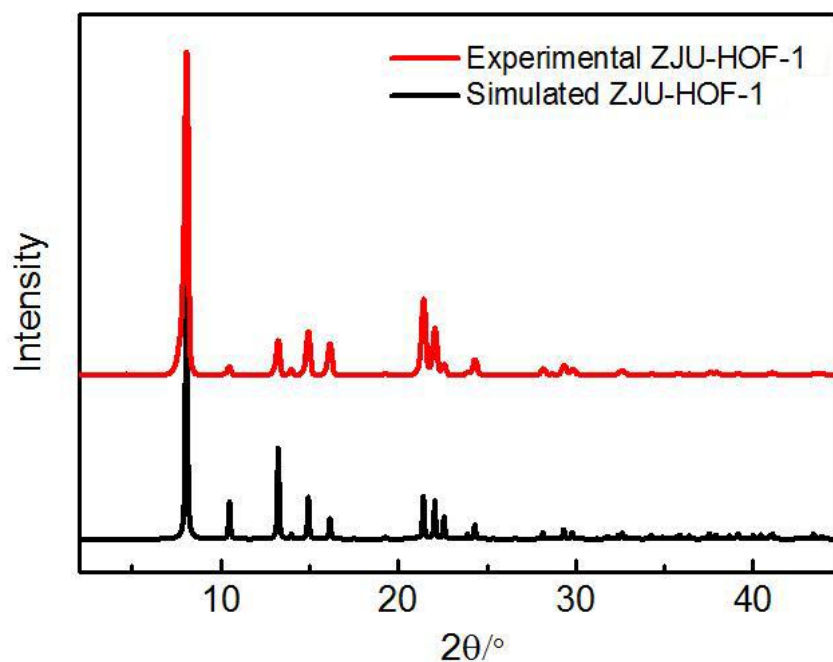


Figure S10. PXRD patterns of experimental activated ZJU-HOF-1 (red) compared with the calculated XRD pattern from the structural model of ZJU-HOF-1 (black), strongly confirming that its validity of the simulated ZJU-HOF-1 structural model.

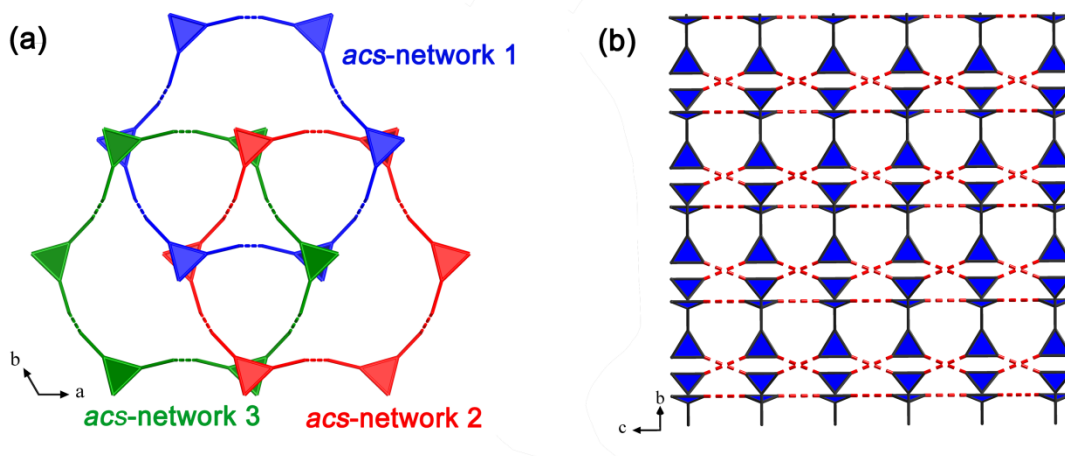


Figure S11. (a) The *acs*-network of ZJU-HOF-1 with 3-fold interpenetration, viewed along the *c* axis and (b) viewed along the *a* or *b* axis.

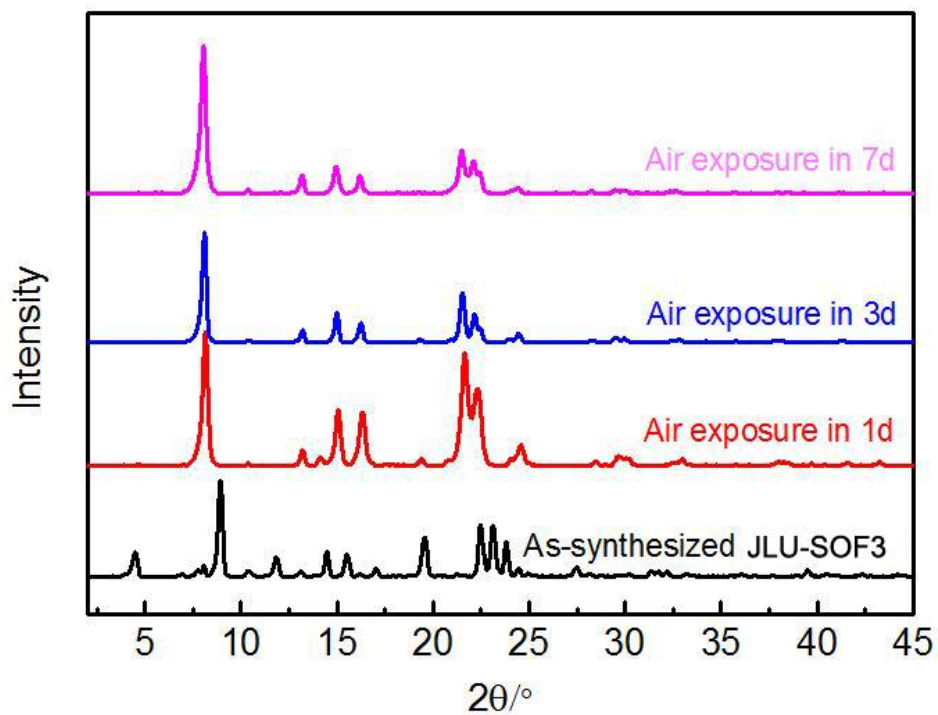


Figure S12. PXRD patterns of as-synthesized samples after exposed to air for 7 days, indicating that the framework can transfer to the activated ZJU-HOF-1 after the guest solvents evaporate away.

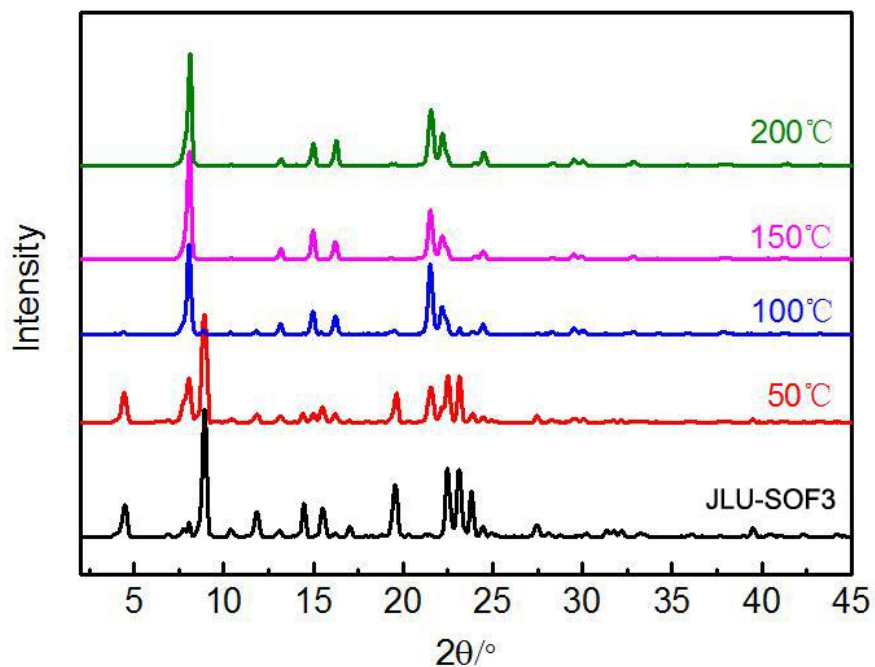


Figure S13. Variable-temperature PXRD patterns for the as-synthesized sample, indicating that the framework can transfer to that of ZJU-HOF-1 after the guest solvents evaporate away by heating.

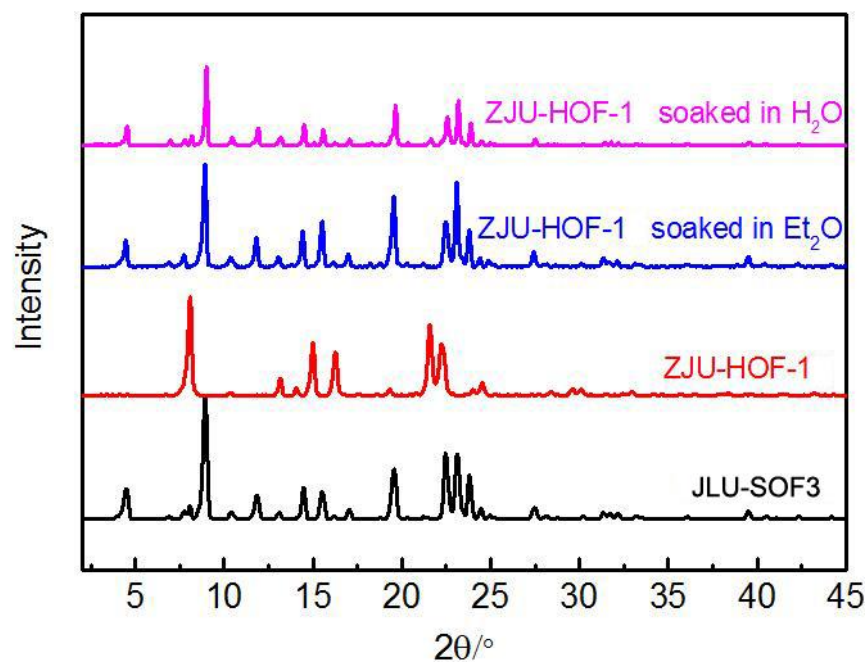


Figure S14. PXRD patterns for ZJU-HOF-1 after soaking in the Et₂O and H₂O, indicating that the framework of ZJU-HOF-1 can reversibly transfer to JLU-SOF3.

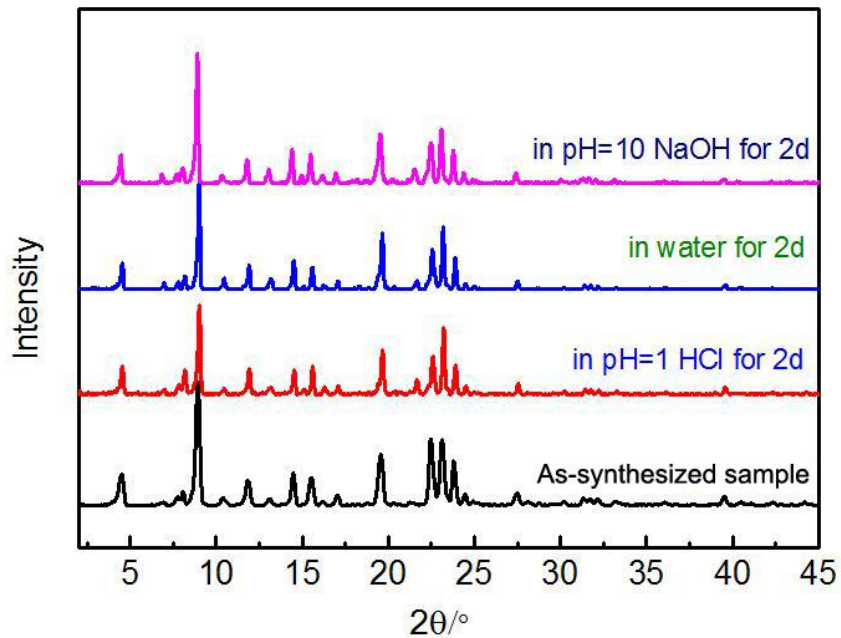


Figure S15. PXRD patterns for the as-synthesized sample after treatment with water, HCl (pH 1) and NaOH (pH 10) solution for 2 days, respectively, exhibiting the excellent chemical stability of the framework.

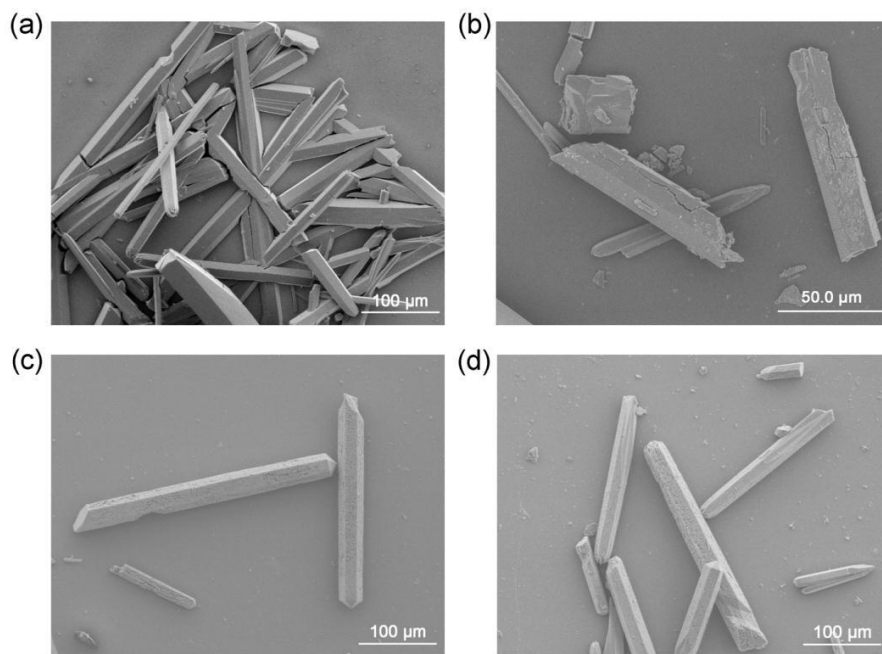


Figure S16. SEM images of (a) the as-synthesized sample; (b) the activated ZJU-HOF-1 sample; (c) as-synthesized sample treated with pH = 1 HCl solution and (d) pH = 10 NaOH solution.

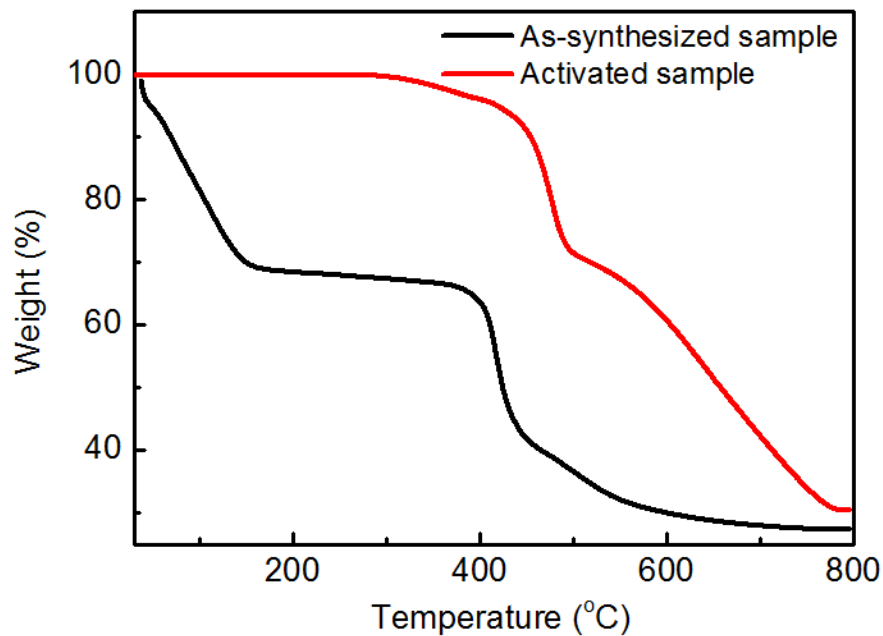


Figure S17. TGA curve of the as-synthesized sample (black) and the activated ZJU-HOF-1 (red), indicating the obvious weight loss before 150 °C due to the guest solvent removal.

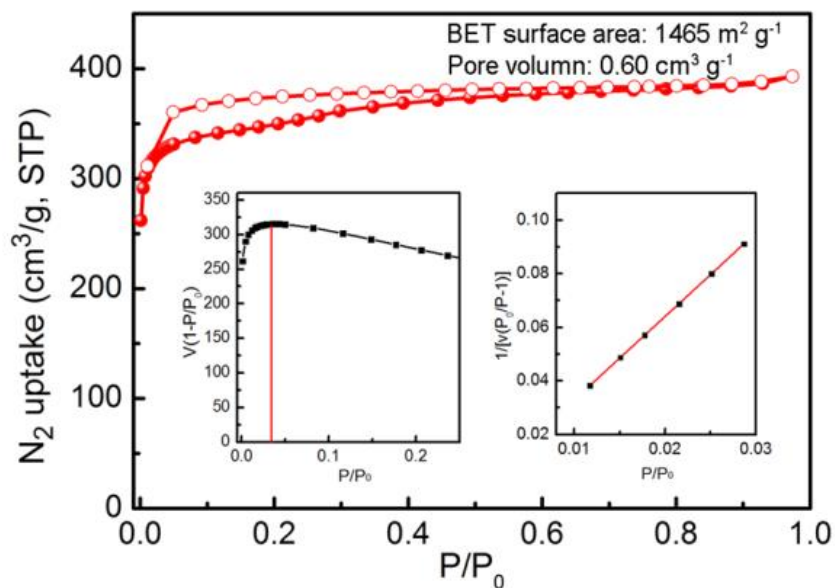


Figure S18. Nitrogen isotherm at 77 K with consistency and BET plots for the activated ZJU-HOF-1 sample.

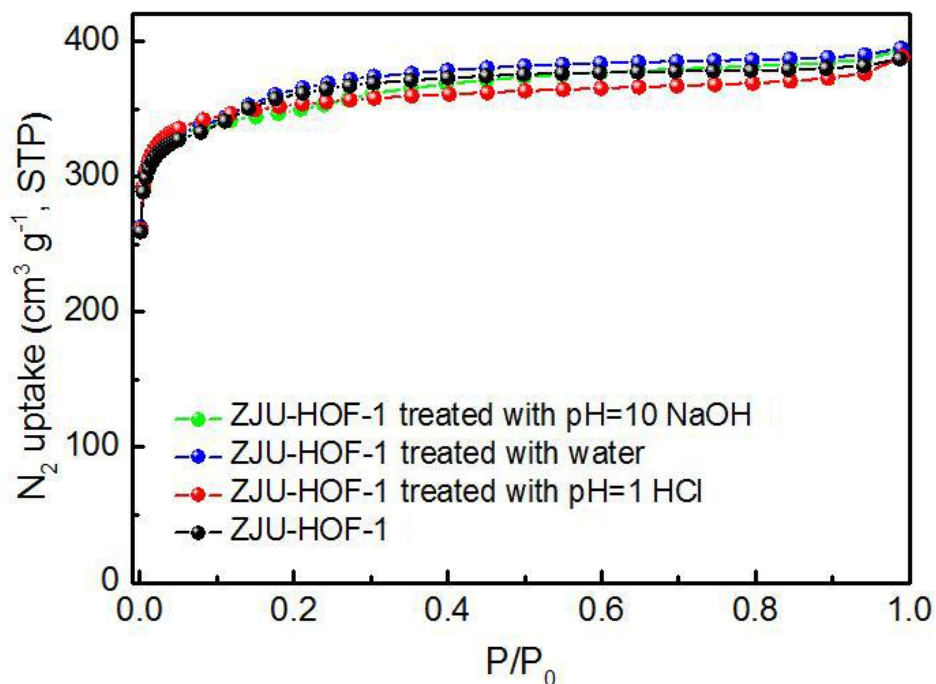


Figure S19. N_2 adsorption isotherms (77 K) of ZJU-HOF-1 and the re-activated samples treated with water, HCl (pH 1) and NaOH (pH 10) solution for 2 days, respectively, indicating its excellent chemical stability.

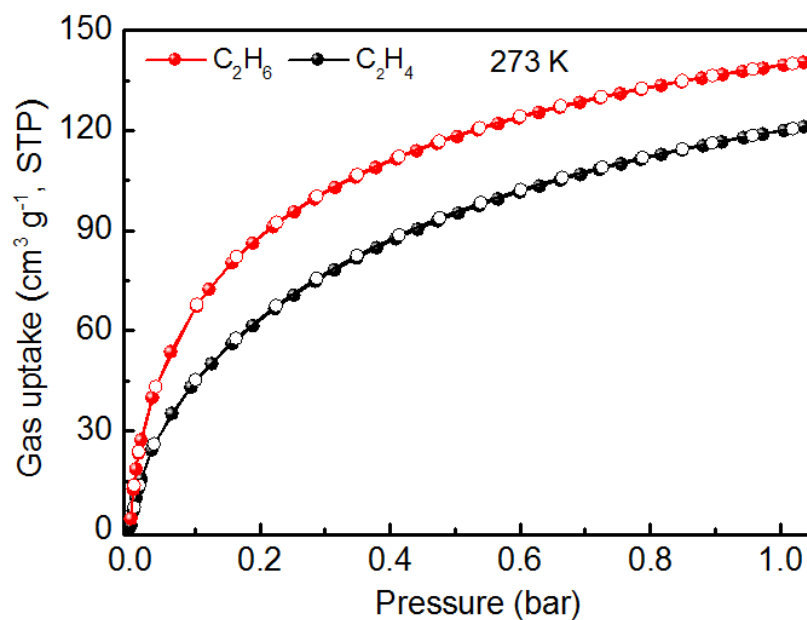


Figure S20. Adsorption isotherms of C_2H_6 (red) and C_2H_4 (black) for ZJU-HOF-1 at 273 K up to 1 bar. Filled/empty symbols represent adsorption/desorption.

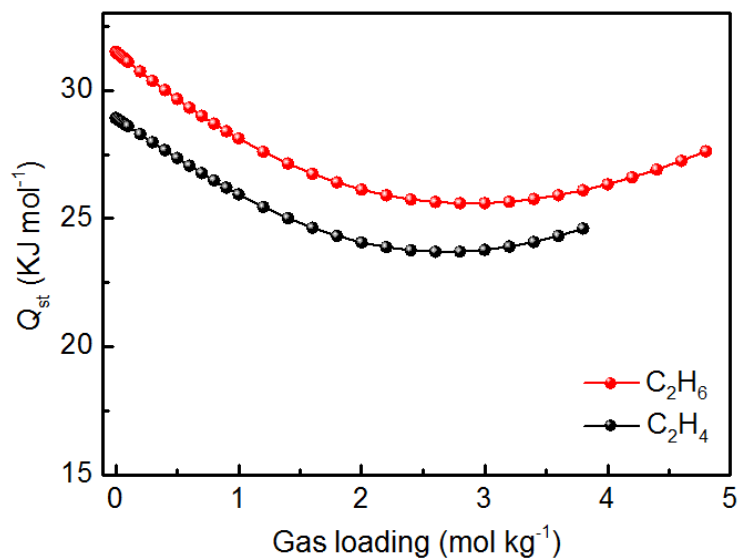


Figure S21. Adsorption heat of the C₂H₆ (red) and C₂H₄ (black) for ZJU-HOF-1.

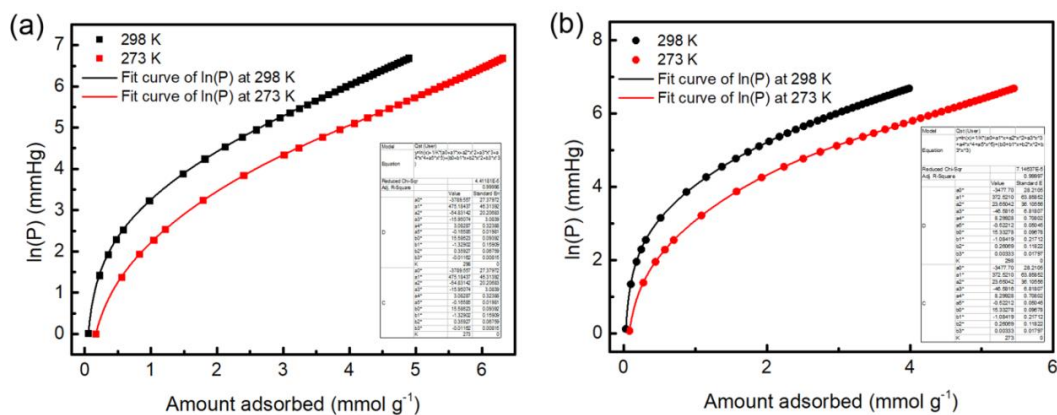


Figure S22. Virial fitting of the C₂H₆ (a) and C₂H₄ (b) adsorption isotherms for ZJU-HOF-1.

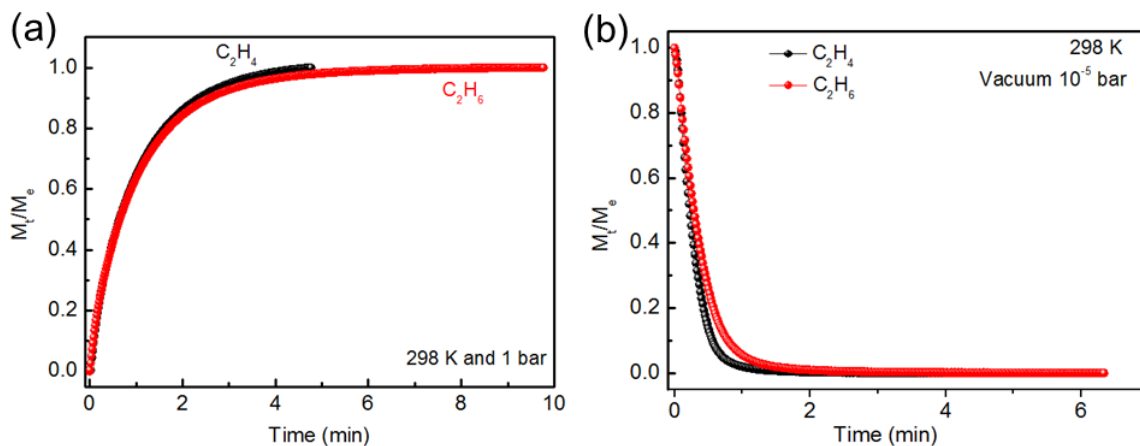


Figure S23. (a) Adsorption kinetics profiles of C₂H₄ (black) and C₂H₆ (red) for ZJU-HOF-1 at 298 K. (b) Desorption kinetics profiles of C₂H₄ (black) and C₂H₆ (red) for ZJU-HOF-1 at 298 K.

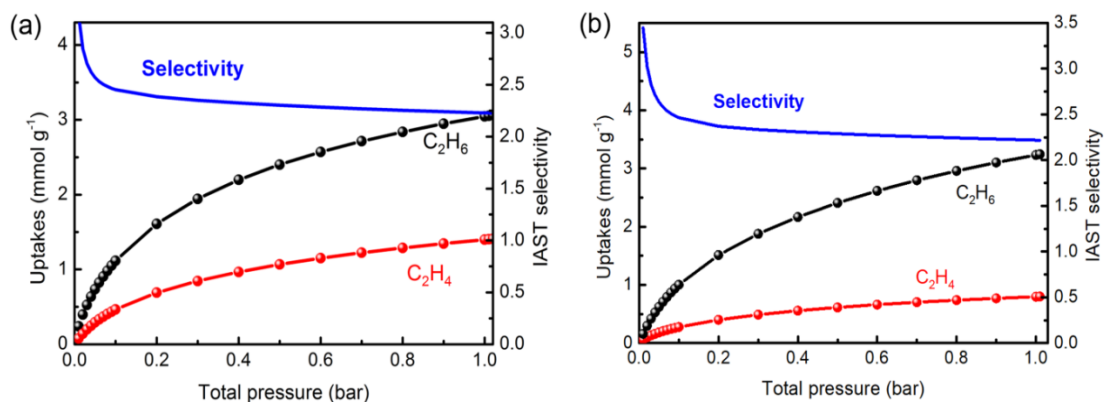


Figure S24. Predicted mixture adsorption isotherms and selectivity of ZJU-HOF-1 predicted by the IAST method for (a) 50/50 (v/v) C₂H₆/C₂H₄ and (b) 10/90 C₂H₆/C₂H₄ mixtures at 298 K.

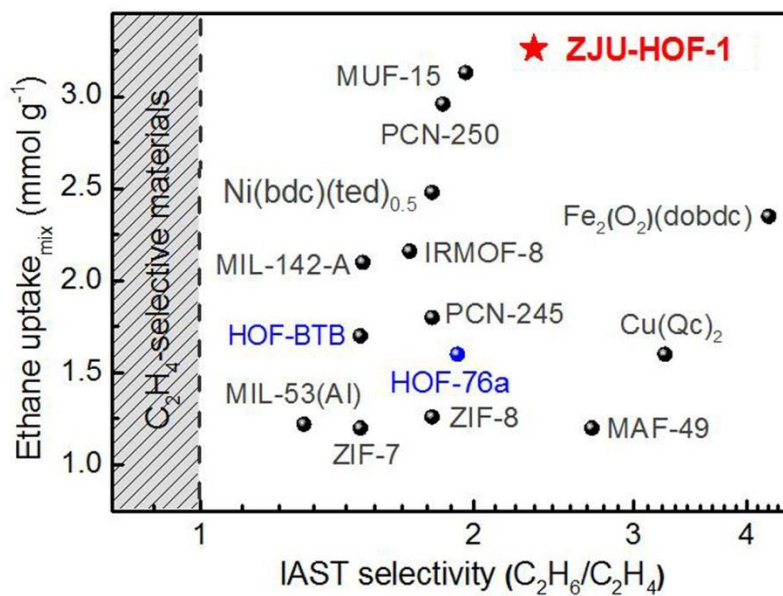


Figure S25. Ethane uptake from an equimolar mixture of C₂H₆/C₂H₄ (50/50) as a function of IAST selectivity calculation at 1 bar and RT for the top-performing C₂H₆-selective materials reported to date, indicating that ZJU-HOF-1 shows the most balanced high C₂H₆ uptake and selectivity from C₂H₆/C₂H₄ gas mixtures.

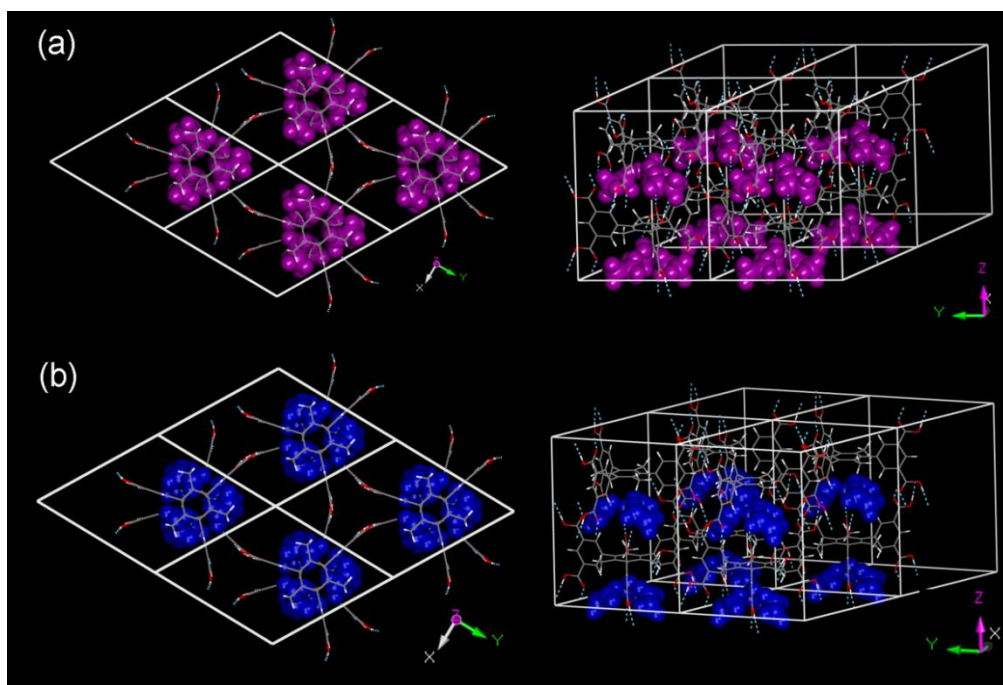


Figure S26. A local structure of ZJU-HOF-1 showing all the adsorbed gas molecules for (a) C₂H₆ and (b) C₂H₄. There exist six gas molecules within each unit cell if all the binding sites are fully occupied.

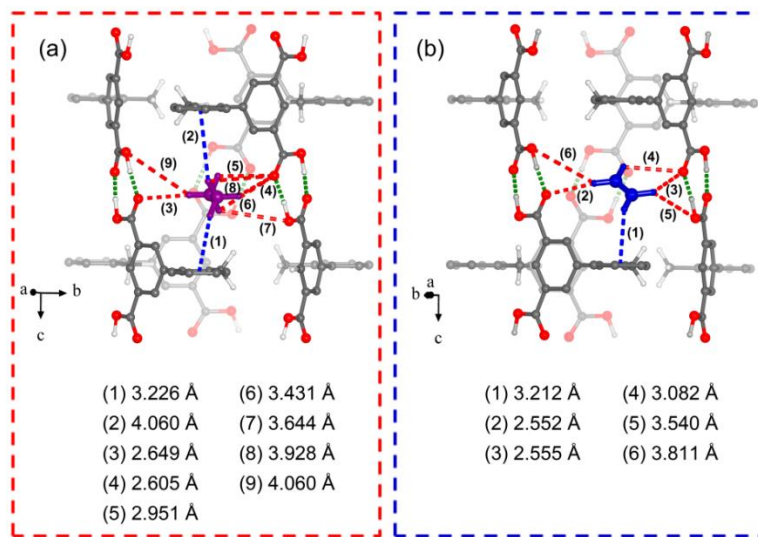


Figure S27. Comparison of the preferential (a) C₂H₆ and (b) C₂H₄ adsorption sites and the close vdW contacts within the pocket pores in ZJU-HOF-1 observed by DFT calculations (C, dark gray; O, red; H, white), highlighting the number and distance of the C–H··· π and C–H···O interactions.

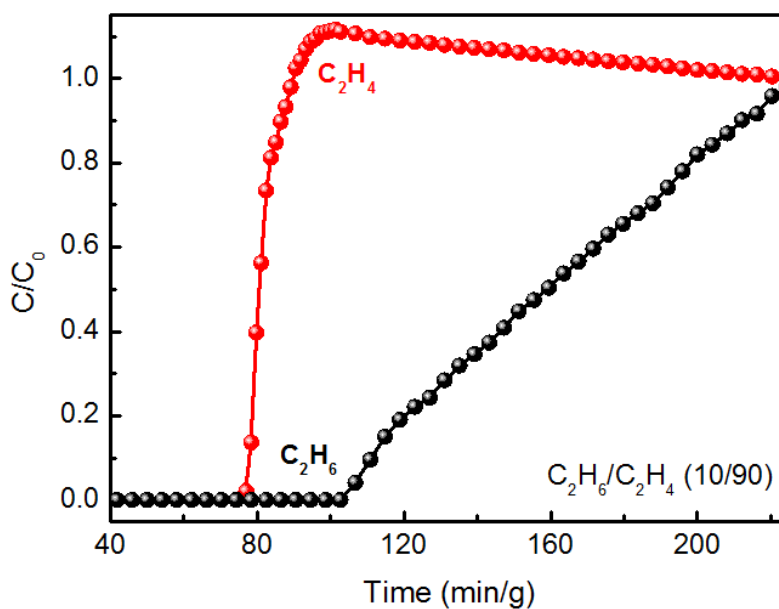


Figure S28. Experimental column breakthrough curves for a 10/90 C₂H₆/C₂H₄ mixture with a total flow of 1.25 mL min⁻¹ in an absorber bed packed with ZJU-HOF-1 at 298 K and 1.01 bar.

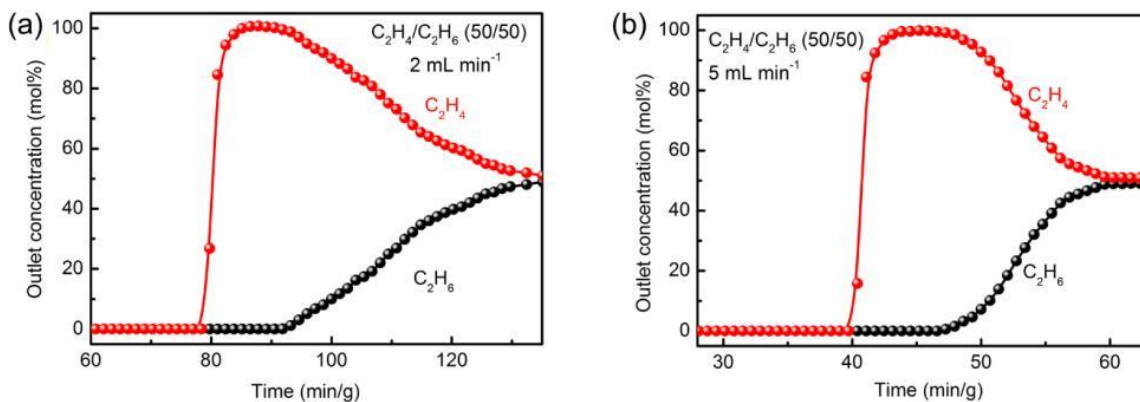


Figure S29. Experimental column breakthrough curves for a 50/50 C_2H_6/C_2H_4 mixture with a total flow of (a) 2 mL min^{-1} and (b) 5 mL min^{-1} in an absorber bed packed with ZJU-HOF-1 at 298 K and 1.01 bar. The pure C_2H_4 ($> 99.95\%$) production was calculated to be 0.95 mmol/g and 1.12 mmol/g , respectively.

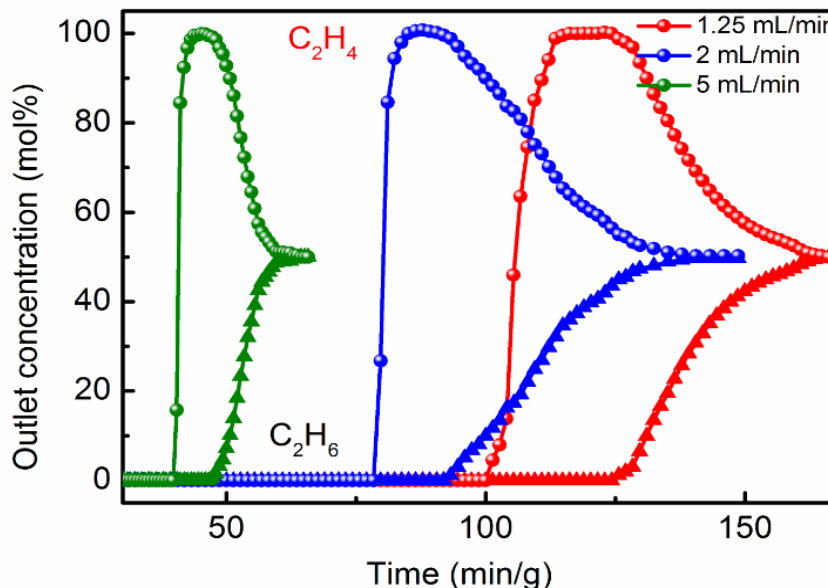


Figure S30. Experimental breakthrough curves for a 50/50 C_2H_6/C_2H_4 mixture at different gas flow of 1.25 mL/min (red), 2 mL/min (blue) and 5 mL/min (green), respectively. With the flow increases from 1.25 to 5 mL/min , both C_2H_4 and C_2H_6 breakthrough time move forward significantly because of the larger gas flow to result in faster adsorption saturation. However, pure C_2H_4 productivity of ZJU-HOF-1 shows no decrease under different gas flow (0.98 mmol/g at 1.25 mL/min , 0.95 mmol/g at 2 mL/min , and 1.12 mmol/g at 5 mL/min).

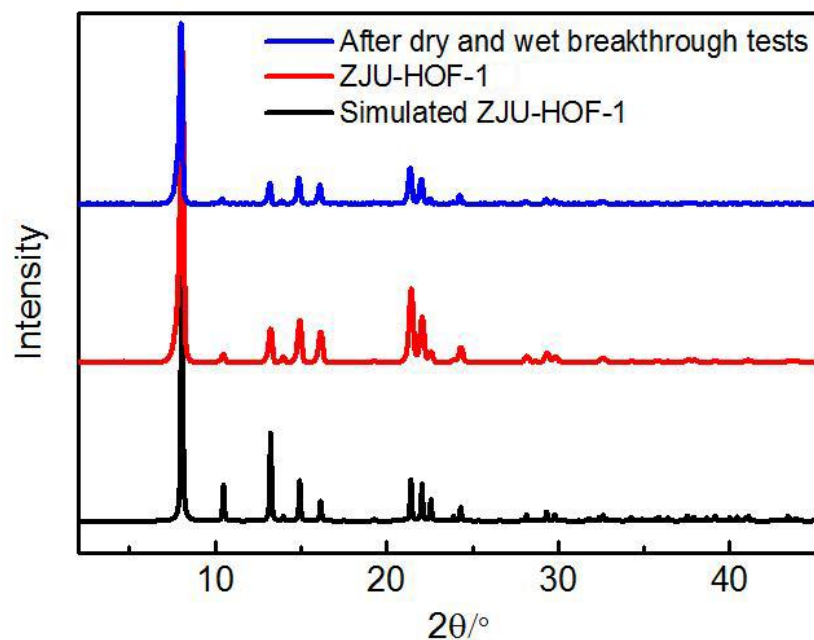


Figure S31. PXRD patterns of simulated ZJU-HOF-1 (black), ZJU-HOF-1 (red), and the samples after the multiple breakthrough tests (blue) under dry and wet gas mixtures.

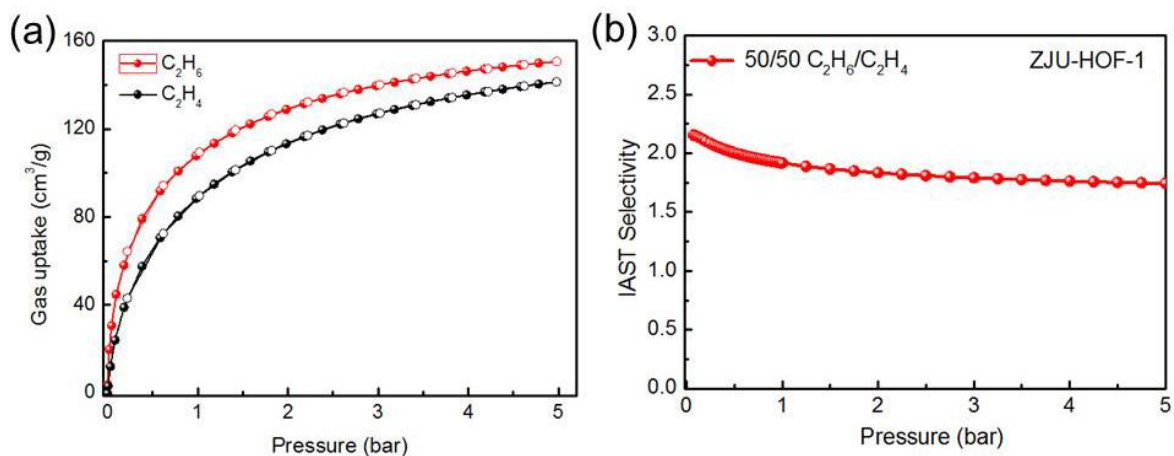


Figure S32. (a) Adsorption isotherms of C_2H_6 (red) and C_2H_4 (black) for ZJU-HOF-1 at 298 K up to 5 bar. (b) IAST selectivity of ZJU-HOF-1 from C_2H_6/C_2H_4 (50/50) gas mixtures up to 5 bar, calculated on C_2H_6 and C_2H_4 high-pressure adsorption isotherms at 298 K.

Disclaimer: Certain commercial suppliers are identified in this paper to foster understanding. Such identification does not imply recommendation or endorsement by the National Institute of Standards and Technology, nor does it imply that the materials or equipment identified are necessarily the best available for the purpose.

REFERENCES

- [1] K. Kobayashi, N. Kobayashi, *J Org. Chem.* **2004**, *69*, 2487-2497.
- [2] G. M. Sheldrick, *SHELXL-97, Program for the refinement of crystal structures*; University of Göttingen: Göttingen, Germany, **1997**.
- [3] L. Li, H.-M. Wen, C. He, R.-B. Lin, R. Krishna, H. Wu, W. Zhou, J. Li, B. Li, B. Chen, *Angew. Chem. Int. Ed.* **2018**, *57*, 15183.
- [4] (a) H.-M. Wen, L. Li, R.-B. Lin, B. Li, B. Hu, W. Zhou, J. Hu, B. Chen, *J. Mater. Chem. A* **2018**, *6*, 6931–6937; (b) G. Xu, B. Li, H. Wu, W. Zhou, B. Chen, *Cryst. Growth Des.* **2017**, *17*, 4795–4800.
- [5] P. Giannozzi, S. Baroni, N. Bonini, M. Calandra, R. Car, C. Cavazzoni, D. Ceresoli, G. L. Chiarotti, M. Cococcioni, I. Dabo, A. Dal Corso, S. Fabris, G. Fratesi, S. de Gironcoli, R. Gebauer, U. Gerstmann, C. Gougoussis, A. Kokalj, M. Lazzeri, L. Martin-Samos, N. Marzari, F. Mauri, R. Mazzarello, S. Paolini, A. Pasquarello, L. Paulatto, C. Sbraccia, S. Scandolo, G. Sclauzero, A. P. Seitsonen, A. Smogunov, P. Umari, R. M. Wentzcovitch, *J. Phys.: Condens. Matter* **2009**, *21*, 395502.
- [6] V. Barone, M. Casarin, D. Forrer, M. Pavone, M. Sami, A. J. Vittadini, *J. Comput. Chem.* **2009**, *30*, 934.
- [7] R. Krishna, *RSC Adv.* **2017**, *7*, 35724–35737.
- [8] R. Krishna, *Sep. Purif. Technol.* **2018**, *194*, 281–300.
- [9] R. Krishna, *Microporous Mesoporous Mater.* **2014**, *185*, 30–50.
- [10] R. Krishna, *RSC Adv.* **2015**, *5*, 52269–52295.
- [11] X. Zhang, L. Li, J.-X. Wang, H.-M. Wen, R. Krishna, H. Wu, W. Zhou, Z.-N. Chen, B. Li, G. Qian, B. Chen, *J. Am. Chem. Soc.* **2020**, *142*, 633–640.
- [12] T.-U. Yoon, S. B. Baek, D. Kim, E.-J. Kim, W.-G. Lee, B. K. Singh, M. S. Lah, Y.-S. Bae, K. S. Kim, *Chem. Commun.* **2018**, *54*, 9360–9363.